Monthly Notices
of the
ROYAL ASTRONOMICAL SOCIETY

MNRAS **509,** 4149–4170 (2022)
Advance Access publication 2021 November 10

https://doi.org/10.1093/mnras/stab3251

# Gas infall and radial transport in cosmological simulations of milky way-mass discs

Cameron W. Trapp [1]★ Dušan Kereš,[1] Tsang Keung Chan [1,2] Ivanna Escala [3,4]† Cameron Hummels,[5] Philip F. Hopkins [5] Claude-André Faucher-Giguère [6] Norman Murray,[7,8] Eliot Quataert[3] and Andrew Wetzel [9]

[1]*Center for Astrophysics and Space Sciences (CASS), University of California San Diego, 9500 Gilman Dr, La Jolla, CA 92093, USA*
[2]*Institute for Computational Cosmology, Durham University, South Road, Durham DH1 3LE, UK*
[3]*Department of Astrophysical Sciences, Princeton University, Princeton, NJ 08544, USA*
[4]*The Observatories of the Carnegie Institution for Science, 813 Santa Barbara St, Pasadena, CA 91101, USA*
[5]*TAPIR, Mailcode 350-17, California Institute of Technology, Pasadena, CA 91125, USA*
[6]*Department of Physics and Astronomy and CIERA, Northwestern University, 1800 Sherman Ave, Evanston, IL 60201, USA*
[7]*Canadian Institute for Theoretical Astrophysics, 60 St. George Street, University of Toronto, ON M5S 3H8, Canada*
[8]*Canada Research Chair in Astrophysics , 60 St. George Street, University of Toronto, ON M5S 3H8, Canada*
[9]*Department of Physics and Astronomy, University of California, Davis, CA 95616, USA*

Accepted 2021 October 31. Received 2021 October 27; in original form 2021 May 24

## ABSTRACT

Observations indicate that a continuous supply of gas is needed to maintain observed star formation rates in large, discy galaxies. To fuel star formation, gas must reach the inner regions of such galaxies. Despite its crucial importance for galaxy evolution, how and where gas joins galaxies is poorly constrained observationally and rarely explored in fully cosmological simulations. To investigate gas accretion in the vicinity of galaxies at low redshift, we analyse the FIRE-2 cosmological zoom-in simulations for 4 Milky Way mass galaxies ($M_{\rm halo} \sim 10^{12} M_{\odot}$), focusing on simulations with cosmic ray physics. We find that at $z \sim 0$, gas approaches the disc with angular momentum similar to the gaseous disc edge and low radial velocities, piling-up near the edge and settling into full rotational support. Accreting gas moves predominately parallel to the disc and joins largely in the outskirts. Immediately prior to joining the disc, trajectories briefly become more vertical on average. Within the disc, gas motion is complex, being dominated by spiral arm induced oscillations and feedback. However, time and azimuthal averages show slow net radial infall with transport speeds of 1–3 km s$^{-1}$ and net mass fluxes through the disc of $\sim$M$_{\odot}$ yr$^{-1}$, comparable to the galaxies' star formation rates and decreasing towards galactic centre as gas is sunk into star formation. These rates are slightly higher in simulations without cosmic rays (1–7 km s$^{-1}$, $\sim$4–5 M$_{\odot}$ yr$^{-1}$). We find overall consistency of our results with observational constraints and discuss prospects of future observations of gas flows in and around galaxies.

**Key words:** stars: formation – galaxies: evolution – galaxies: kinematics and dynamics – galaxies: spiral.

## 1 INTRODUCTION

Massive disc galaxies, including our own Milky Way, show relatively stable star formation rates (SFRs) over the past few Gyr (Binney, Dehnen & Bertelli 2000) and actively form stars over cosmic time. Such star formation cannot be solely supplied by existing gas reservoirs in the interstellar medium (ISM), as measured gas depletion times are too short for sustained star formation. Typical depletion times of molecular gas ($t_{\rm dep} = {\rm M_{H_2}/SFR}$) are $\sim$1–2 Gyr at present time and even shorter at higher redshift (Saintonge et al. 2017; Tacconi et al. 2018). In large, discy galaxies such as the Milky Way (MW), more extended neutral hydrogen reservoirs can condense to $H_2$ and continue fuelling star formation, but these would still deplete within $\sim$2 Gyr (Kennicutt 1998). Given that these depletion times are an order of magnitude shorter than the Hubble time ($\sim$14 Gyr), these reservoirs must be resupplied over time. Gas recycling via stellar mass-loss (Leitner & Kravtsov 2011) can provide a partial source, but a continuous supply of gas is still necessary to maintain observed SFRs.

More local observations, such as the G-Dwarf problem (i.e. the relative scarcity of low metallicity stars in the solar vicinity does not match predictions from simple galactic chemical evolution models) (van den Bergh 1962; Schmidt 1963; Sommer-Larsen 1991; Worthey, Dorman & Jones 1996; Haywood et al. 2019), additionally motivate the need for continuous accretion of low metallicity gas from the circumgalactic medium (CGM) in present day discs.

One of the most direct ways to account for this accretion is through observation of intermediate- and high-velocity clouds (IVCs and HVCs). IVCs and HVCs are gaseous clouds with strong kinematic deviations from galactic rotation, so this classification selects gas that is not yet part of the rotationally supported disc. These deviations are typically within 40–70 km s$^{-1}$ for IVCs, and

★ E-mail: ctrapp@ucsd.edu
† Carnegie-Princeton Fellow

above 70–90 km s$^{-1}$ for HVCs (Röhser et al. 2016). Observations of HVCs around the MW have shown total gas accretion rates of around 0.4 M$_\odot$ yr$^{-1}$, which is not enough to fully support observed SFRs of ∼2–3 M$_\odot$ yr$^{-1}$ (Putman, Peek & Joung 2012). IVC accretion is likely related to galactic fountain recycling (Putman et al. 2012) and may provide a significant fraction of total accretion (Röhser et al. 2016), however, further observational studies are required.

The nature of gas accretion over cosmic time from the intergalactic medium to galactic regions has been extensively studied in hydrodynamic galaxy formation simulations. Broadly speaking, cosmological simulations show that star formation is largely supply driven and typical accretion rates are on the order of galactic star formation rates (e.g. Kereš et al. 2005). Additionally, simulations found that gas can accrete in 'cold-mode', along filamentary streams, where gas does not shock to the virial temperature in the outer halo (Kereš et al. 2005; Dekel & Birnboim 2006; Ocvirk, Pichon & Teyssier 2008; Brooks et al. 2009; Kereš et al. 2009; Faucher-Giguère, Kereš & Ma 2011; van de Voort et al. 2011a; Stern et al. 2021). Such accretion dominates at early times, while at late times and/or in more massive haloes cooling from the hot halo gas ('hot-mode') can be more important. The present-day Milky Way is expected to be in the 'hot mode' regime, but close to the mass where the transition between these two cases occurs (Kereš et al. 2005; Dekel & Birnboim 2006; Ocvirk et al. 2008; van de Voort et al. 2011b; Nelson et al. 2013; Stern et al. 2020), and it is therefore especially interesting. Furthermore, when stellar feedback and resulting galactic outflows are included, a significant fraction of late time accretion originates from previous episodes of gas ejection from galaxies (Oppenheimer et al. 2010; Muratov et al. 2015; Wetzel & Nagai 2015; Anglés-Alcázar et al. 2017; Hafen et al. 2017). Further investigation of accretion in the context of cold mode/hot mode in the FIRE simulations is the subject of upcoming work (Hafen et al., in preparation).

Simulations also suggest that high-redshift gas accretion can corotate with the discs near the edge of the stellar disc (Kereš et al. 2005; Danovich et al. 2015; Stewart et al. 2017). However, high accretion rates and the resulting strong stellar feedback and outflows lead to relatively chaotic discs with high velocity dispersion and strong time variations in infalling gas (e.g. Muratov et al. 2015). This picture changes at later times in Milky Way-mass galaxies: infall is steady while outflows are weaker, facilitating formation of coherent discs (e.g. Kassin et al. 2012; Muratov et al. 2015; Stern et al. 2021). This enables characterization of the gas infall with respect to the disc plane.

Numerical simulations show that accreting cold gas is largely corotating at late times (Kereš & Hernquist 2009; Stewart et al. 2011; Ho, Martin & Turner 2019). Given the large specific angular momentum of overall halo gas (El-Badry et al. 2018), accreting gas can settle into rotational support in the disc outskirts regardless of its temperature history. This is consistent with the standard picture, where galactic discs grow inside-out (Fall & Efstathiou 1980).[1] There is also indirect observational support for this scenario from larger scale gas flows, where cold/warm absorbers in haloes of low redshift galaxies show corotation with the disc, potentially mapping such infalling gas (Diamond-Stanic et al. 2016; Muzahid et al. 2016; Bielby et al. 2017; Péroux et al. 2017). Studies at higher redshifts utilizing background quasars to probe disc outskirts have also shown kinematic evidence for co-rotating structures out to 30–60 kpc (Barcons, Lanzettat & Webb 1995; Bouché et al. 2013; Zabl et al. 2019).

If this is the main way in which our own Galaxy accretes gas, it makes it hard to kinematically distinguish accreting gas from the gas already in the disc. This also suggests that a large fraction of accretion is not in HVCs, explaining the fact that HVC accretion rates are much lower than what is needed to fuel observed SFR. Several studies have explored inflow from mostly co-rotating gas, though interpreting observed gas kinematics and inflow solely from the observed Doppler shift is difficult and can lead to large uncertainties (Wong, Blitz & Bosma 2004; Martin et al. 2012; Rubin et al. 2012; Ho & Martin 2020). Robust theoretical predictions for the nature of gas infall close to galaxies are clearly needed to test this scenario and guide future observations.

While our expectations are that gas will join the disc in the outskirts, most of the galactic star formation occurs in the inner regions. This means that an efficient transport mechanism is needed for gas to move from disc outskirts inward. Several theoretical studies have explored radial gas transport within the disc (e.g. Dekel, Sari & Ceverino 2009; Krumholz & Burkert 2010; Krumholz et al. 2018; Forbes, Krumholz & Speagle 2019) and the radial migration of clumps through the disc at higher redshifts in cosmological simulations (e.g. Ceverino, Dekel & Bournaud 2010; Hopkins et al. 2012; Mandelker et al. 2014; Oklopčić et al. 2017). However, radial transport velocity and mass flux of gas have not been explored in great detail in fully cosmological simulations of disc galaxies. On the other hand, observational studies searching for the radial gas flows within the disc are rare and inconclusive (Wong et al. 2004; Schmidt et al. 2016).

Our goal in this paper is to clarify the theoretical picture of galactic gas infall and radial gas transport in Milky Way-mass galaxies at late times and provide predictions to guide future observations of these processes. For this purpose, we utilize outputs from a subset of new FIRE-2 (Feedback In Realistic Environments)[2] cosmological zoom-in simulations, which in addition to explicit stellar feedback models, incorporate magnetohydrodynamics and cosmic ray physics (CR+; Chan et al. 2019; Hopkins et al. 2020). A key parameter in these simulations – the effective diffusion coefficient of cosmic rays – was previously constrained based on observed galactic gamma-ray emission (Lacki et al. 2011). We focus on $0 < z < 0.2$; this is the time when stable, thin, discs with clear orientation exist, enabling us to make robust predictions both externally and from the perspective within the disc. We characterize (i) the net accretion rates, star formation rates, and radial gas transport rates within the disc. We also characterize (ii) the directionality (i.e. parallel to the disc) of gas flow as it accretes on to the disc, (iii) the evolution of angular momentum of gas particles as they accrete, (iv) the radius at which particles join the disc, and (v) what happens to particles when they join the disc. Finally, we discuss the viability of observing these flows and compare these results with the hydrodynamical only (Hydro+) FIRE-2 runs and runs with magnetohydrodynamics but no CR physics (MHD+). CR+ runs were chosen for the main analysis due to their more realistic late time star formation compared to Hydro+ and MHD+ runs (Hopkins et al. 2020). A more detailed analysis of the phase evolution of accreting and transporting gas will be done in future work.

[1] If halo gas has significant non-thermal pressure support from cosmic rays, infall geometry might be even more confined to galactic plane (Hopkins et al. 2021a).

[2] http://fire.northwestern.edu

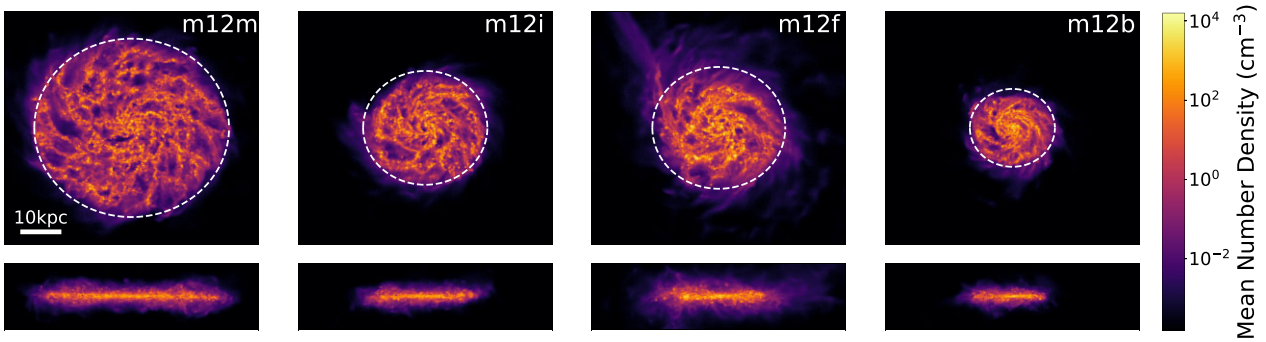


**Figure 1.** Mean gas density along line of sight for the four galaxies in our sample at redshift z = 0. The white dashed lines show the radius where the neutral hydrogen column density drops below $10^{20.3}$ cm$^{-2}$ ($R_{\rm DLA}$, see Table 1). All four galaxies exhibit clear, thin gaseous discs. The disc in **m12f** underwent a recent merger event with an LMC like object at redshift 0.08, resulting in the streaming accretion feature in the top left quadrant and affecting numerous metrics in our analysis.

Section 2 describes the simulations used in detail. Section 3 describes the processing techniques used to analyse the data. Section 4 provides the key results from our simulation analysis. Section 5 discusses the significance of our findings and introduces basic observational predictions. Appendix A compares the CR+ runs presented in the main paper with the Hydro+ and MHD+ runs, Appendix B contains supplementary figures to the main text, and Appendix C compares simulations run at different mass resolution.

## 2 SIMULATIONS

This study is based on 4 simulated Milky Way-mass discy galaxies evolved in cosmological context (see Fig. 1 for face-on and edge-on view of their gaseous discs) where gas infall, large and small scale outflows and galaxy interactions are modelled self-consistently. Simulations utilize 'zoom-in' technique to reach high resolution in fully cosmological settings and were run with the gravity+(magneto)hydrodynamics code GIZMO (Hopkins 2015) using mesh-free Lagrangian Godunov (meshless finite mass, MFM) method.

Cooling, star formation, and stellar feedback are implemented as in FIRE-2 (Hopkins et al. 2018), an updated version of the FIRE project (Hopkins et al. 2014). The simulations include photoionization and photoheating from the cosmic UV background based on the Faucher-Giguère et al. (2009) model. Star formation is enabled in self-shielding/molecular, Jean unstable dense ($n_{\rm H} > 1000\,{\rm cm}^{-3}$) gas. Once created, star particles are treated as single-age stellar populations with IMF-averaged feedback properties calculated from STARBURST99 (Leitherer et al. 1999) assuming a Kroupa (2001) IMF. Feedback from SNe (Type Ia and II), stellar mass-loss (O/B and AGB), and radiation (photoionization, photoelectric heating, and UV/optical/IR radiation pressure) are explicitly treated as in Hopkins et al. (2018). In this analysis, we use simulations that in addition to standard FIRE-2 feedback incorporate magnetohydrodynamics (MHD) and cosmic ray (CR) physics (Hopkins et al. 2020) using CR transport methodology fully described in Chan et al. (2019). To summarize, runs include CR injection in SNe shocks, fully anisotropic CR transport with streaming, advection, and diffusion, CR losses (hadronic and Coulomb, adiabatic, streaming), and CR-gas coupling.

The FIRE simulations have been successful in matching a range of galactic properties to observations, including total stellar mass; star formation rates and histories (Hopkins et al. 2014; Feldmann et al. 2016; Sparre et al. 2017; Santistevan et al. 2020); dense H I covering fraction in the circumgalactic medium at both low and high redshift (Faucher-Giguère et al. 2015, 2016; Hafen et al. 2017); outflow properties (Muratov et al. 2015, 2017); metallicities (Ma et al. 2016; Bellardini et al. 2021); morphological/kinematic structure of thin/thick discs (Ma et al. 2017; Sanderson et al. 2020; Yu et al. 2021); baryonic and dark matter mass profiles and content within the halo (Chan et al. 2015; Wetzel et al. 2016); Giant molecular cloud properties (Benincasa et al. 2020; Guszejnov et al. 2020); and circular velocity profiles (Hopkins et al. 2018).

In general, our MW-mass galaxies with CRs show good agreement with the observationally inferred $M^*$–$M_{\rm halo}$ relation and are disc dominated (Hopkins et al. 2020). Stellar masses in runs without CRs are somewhat higher than this relation predicts. On the other hand, CR+ runs may be slightly underestimating stellar mass, although statistics are still poor. Our choice of simulations with additional CR physics is mainly guided by their lower late time star formation rates of 2–3 $M_\odot\,{\rm yr}^{-1}$ versus 3–10 $M_\odot\,{\rm yr}^{-1}$ in FIRE-2 simulations without CRs, which is closer to what is seen in the Milky Way. This lower star formation is associated with lower velocity dispersion of galactic discs and potentially additional planar alignment of the accreting gas (Hopkins et al. 2021a). In addition, the circumgalactic medium in MW-mass simulations with CRs is in better agreement with observations of low and intermediate ions seen in absorption systems around galaxies (Ji et al. 2020). We compared the results from our default CR+ runs with simulations without CRs and found that, despite differences in late-time star formation, both default FIRE-2 simulations and CR+ runs show similar qualitative behaviour and trends in gas accretion on to low redshift discs (see Appendix A).

The minimum baryonic particle mass in our simulations is $m_{\rm b,min} = 7100\,M_\odot$ and a typical gravitational force softening for star forming gas is ∼2 pc. Note that spatial resolution (softening and smoothing lengths) for our gas particles is adaptive; typical force softening for ISM gas is ∼20 pc. All simulations employ a standard flat ΛCDM cosmology with $h \approx 0.7$, $\Omega_{\rm M} = 1 - \Omega_\Lambda \approx 0.27$, and $\Omega_{\rm b} \approx 0.046$ (consistent with Planck Collaboration XVI 2014).

## 3 SIMULATION ANALYSIS

In Fig. 2, we show visualizations of the H I and $H_2$ column densities viewed face and edge for our four simulated galaxies; a basic summary of their relevant properties is presented in Table 1. We define the radius of each galaxy as the radius where the face-on, azimuthally averaged neutral hydrogen column density drops below $10^{20.3}\,{\rm cm}^{-2}$ ($R_{\rm DLA}$), the column density limit of Damped

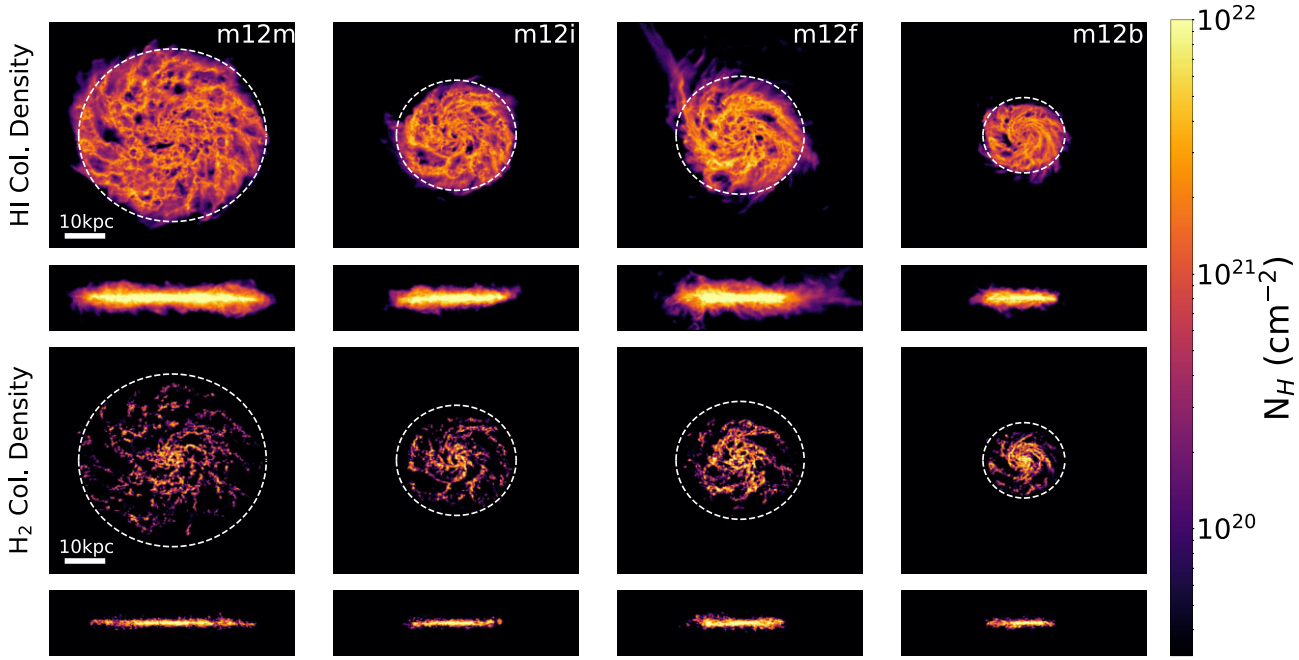


**Figure 2.** Neutral (H I) and molecular ($H_2$) hydrogen column densities for the four galaxies in our sample. The white dashed lines show the radius of the disc ($R_{DLA}$, Table 1). H I drops off sharply outside the disc. Molecular hydrogen is more concentrated towards the galactic centre.

**Table 1.** Parameters characterizing the size of the disc for the four galaxies in our sample at z = 0. $R_{vir}$ is the virial radius (calculated following Bryan & Norman 1998). $R_{*,1/2}$ is the radius at which half the stellar mass is contained. $R_{DLA}$ is the radius at which the total hydrogen column density drops below $10^{20.3}$ cm$^{-2}$ when viewed face on, signifying the transition to a column density below a Damped Lyman Alpha (DLA) system. Likewise, $R_{HI,19}$ is the radius at which the H I column density drops below $10^{19}$ cm$^{-2}$. $h_{total}$ is the scale height of the total gas and $h_{cold,inner}$ is the scale height of the cold hydrogen ($T < 100$ K) in the inner 5 kpc. Scale height was calculated as the height the average gas density drops by a factor of $e$ from the average value within ±20 pc of the mid-plane. The parameter $t_{orbit}$ is the dynamical time of the galaxy, defined as the average orbital period of disc gas within a 1 kpc bin centred at $R_{DLA}$. The rotational velocity ($v_c$) is the value predicted from the enclosed mass at 0.5 $R_{DLA}$. Full rotation curves for most galaxies in our sample can be found in Hopkins et al. (2020). $M_*$ is the stellar mass contained within 3 $R_{*,1/2}$.

| Simulation Name | $R_{vir}$ (kpc) | $R_{*,1/2}$ (kpc) | $R_{DLA}$ (kpc) | $R_{HI,19}$ (kpc) | $h_{total}$ (kpc) | $h_{cold,inner}$ (kpc) | $t_{orbit}$ (Gyr) | $v_c$ (km s$^{-1}$) | $M_*$ ($M_\odot$) |
|---|---|---|---|---|---|---|---|---|---|
| **m12m** | 232.0 | 7.84 | 26.8 | 30.5 | 0.87 | 0.21 | 0.874 | 190 | 3e10 |
| **m12i** | 215.4 | 3.61 | 17.1 | 20.6 | 0.76 | 0.18 | 0.643 | 178 | 3e10 |
| **m12f** | 237.1 | 3.72 | 18.3 | 28.8 | 1.01 | 0.33 | 0.675 | 193 | 4e10 |
| **m12b** | 221.2 | 1.81 | 11.7 | 15.1 | 0.47 | 0.14 | 0.438 | 206 | 4e10 |

Lyman Alpha (DLA) systems (Wolfe, Gawiser & Prochaska 2005). We additionally provide the radii at which this column density drops below $10^{19}$ cm$^{-2}$. The disc scale height is quantified as the height the average gas density drops by a factor of $e$ from the average value within ±20 pc of the mid-plane. It is quantified in two ways, based on total hydrogen number density ($h_{total}$) as well as cold ($T < 100$ K) hydrogen number density within the inner 5 kpc ($h_{cold,inner}$). We additionally calculate a characteristic time period for each galaxy ($t_{orbit}$) as the rotation period of gas particles at the disc edge. Rotational velocity ($v_c$) was predicted from the enclosed mass at 0.5 $R_{DLA}$. Full rotation curves for most of these galaxies can be found in Hopkins et al. (2020). These values will be used to normalize distances and times in subsequent sections to allow for more direct comparisons between galaxies.

We focus on the gas in late time discs in the redshift interval z = 0.0–0.2, as the discs are thin, stable, and have a clear orientation. For each galaxy, we initially define a cylindrical coordinate system centred on the galactic centre and oriented along the angular momentum vector of the galaxy. We calculate the galactic centre from the mass distribution of the star particles using a shrinking sphere algorithm.[3] We determine the galactic velocity by calculating the mass-weighted velocity average of all star and dark matter particles within 15 kpc of galactic centre. The orientation of the angular momentum vector was determined from the vector sum of angular momenta of cold dense gas particles ($T < 8000$ K, $n > 1$ cm$^{-3}$) in the inner 10 kpc, with respect to the galactic centre. We analyse the gas flow properties through a bulk flow analysis of all gas particles, as well as particle tracking of sub-selections of accreting particles.

[3] A 1 Mpc radius sphere was defined around the region of maximal gas density and the stellar centre of mass was calculated. This sphere was shrunk by a factor of 0.7 and the centre of mass recalculated until it reached a radius of 10 kpc. The centering was repeated without shrinking until the centre converged to a stable value.

### 3.1 Bulk flow analysis

The mass, density, velocity, and position of each gas particle were read from each simulation snapshot. We transformed the position and velocity vectors into the previously defined cylindrical coordinate system and binned the data in order to calculate locally averaged values. Data were binned into a 0.25 × 0.25 × 0.25 kpc Cartesian grid (x,y,z) and into a 0.1 kpc × 0.1$\pi$ rad × 0.25 kpc cylindrical grid (r,$\theta$,z). In order to quantify global gas flow properties, we additionally binned data in 1 kpc spherical radial bins. During analysis, bins were averaged or summed together to create coarser resolution as needed. For each bin, we calculated the total mass, angular momentum, and linear momentum components. We additionally calculated mass-weighted average velocity components and specific angular momenta. We estimated mass flux as follows:

$$\text{Mass Flux} = \frac{1}{\Delta \text{r}} \sum_{\text{i}} \vec{p_i} \cdot \hat{\text{r}}_{\text{i}}, \quad (1)$$

where $\Delta r$ is the size of the radial bin and $\vec{p_i} \cdot \hat{r_i}$ is the $i$th particles momentum component in the radial direction (spherical or cylindrical).

For some of our visualizations and observational predictions we utilize the column densities of total hydrogen, H I, and $H_2$. Neutral hydrogen fraction is calculated using on-the-fly self shielding in FIRE with a local Sobolev/Jeans-length approximation (Hopkins et al. 2018) and is written in the simulation output. We additionally take molecular fraction values directly from the simulations, which were calculated during the simulation runs following the approximation outlined in Krumholz & Gnedin (2011).[4]

Stellar mass distribution and SFR were binned spatially in a similar fashion. For each stellar bin, we calculated the total stellar mass by summing the mass of each star particle in each bin. In order to quantify star formation, we calculated the total mass of newly formed stars, identified as stars formed within 20 Myr. This short time interval minimizes the effects of stellar drift in identifying star formation location (Orr et al. 2018).

### 3.2 Particle tracking

Resolution elements (particles) in the FIRE-2 simulations are uniquely trackable throughout a run, including through particle splitting and star formation events.[5] To characterize the behaviour of individual gas elements as they join the disc and form stars, we defined accreting gas as particles that are present inside the characteristic radius of the disc ($R_{\text{DLA}}$) at z = 0.03 (either as gas or stars), but are located at a distance greater than this radius at redshift z = 0.17. We track particles between redshift z = 0.20 and z = 0.00. The difference from the selection criteria (z = 0.03–0.17) is such that we follow each particle for at least 0.4 Gyr before and after accretion.[6]

[4]FIRE-2 simulations by do not save molecular fraction as an output by default. We therefore reran the simulations at redshift 0 soley to output molecular fraction. The time-step was chosen such that no particles were updated.

[5]Each particle is assigned a particle ID, child ID, and generation number. When a gas particle crosses a certain mass threshold, it is split into two separate particles with unique child IDs and the particles generation number is incremented. Star particles retain the original gas particles IDs.

[6]If multiple particles split from the same parent during this time period, the parent particle is accounted for multiple times. This double counting is corrected for when calculating relevant metrics.

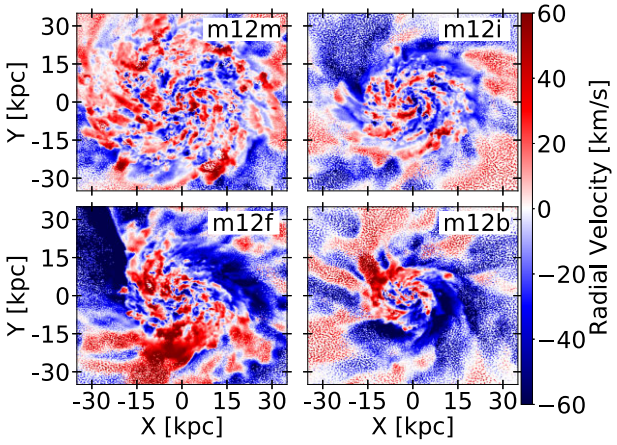


**Figure 3.** Face on views showing averaged cylindrical radial velocities for all gas within 1.5 kpc of the disc plane at z = 0. For a corresponding figure with vertical velocity, see Appendix B. Note the fast inflowing gas in the top right-hand quadrant of **m12f** corresponding to continued accretion from the merger event. All galaxies show clear inflow at radii outside the disc.

At every snapshot, we track each particles' position, momentum, mass, and particle type (gas or star) in order to characterize the kinematics of the accretion process and identify where/when they form stars. We identify when/where a particle joins the disc in 2 ways: (i) geometrically and (ii) by specific angular momentum. In the geometric classification, a particle joins the disc when it passes through a height of $2h_{\text{total}}$ and remains for at least one $t_{\text{orbit}}$. In the specific angular momentum classification, a particle joins the disc when its specific angular momentum reaches within 20 per cent of the rotation curve as predicted by the mass distribution and remains for at least one $t_{\text{orbit}}$. Both of these cutoffs are based on the typical spread of particle heights and angular momenta within the disc. Reducing the time requirement from one $t_{\text{orbit}}$ causes particles to be classified as joining the disc at larger radii on average.

## 4 RESULTS

All four galaxies in our sample (**m12m**, **m12i**, **m12f**, and **m12b**) have large discy structures. In general $H_2$ is centrally concentrated and correlated with spiral arm-like structure, while H I is more smoothly distributed throughout the discs. Typical face-on H I column densities in the disc region are of order $10^{21}$ cm$^{-2}$ and drop off very sharply at the disc edge (Fig. 2). There are some key structural differences of note between galaxies. The disc in **m12m** is much more extended than the other galaxies, while the **m12b** is the most compact. This difference affects location and geometry of the gas accretion and star formation. Additionally, **m12f** has a minor merger at z ∼ 0.1 with an LMC mass object ($M_* = 1.7 \times 10^9$ M$_\odot$).

### 4.1 Global gas flow properties

All galaxies show net inflow at larger radii (Figs 3, 4). The mass flux from this inflow is roughly equivalent to both the radial mass flux through the disc, as well as the total star formation rate of the galaxy (Table 2). Values are not expected to match perfectly owing to low level galactic outflows (Muratov et al. 2015; Pandya et al. 2021) and partial gas supply from stellar mass recycling within the disc. Fig. 3 shows face on maps of cylindrical radial velocity. While there are outward flowing features throughout, the disc outskirts are inflow dominated with significant azimuthal velocity

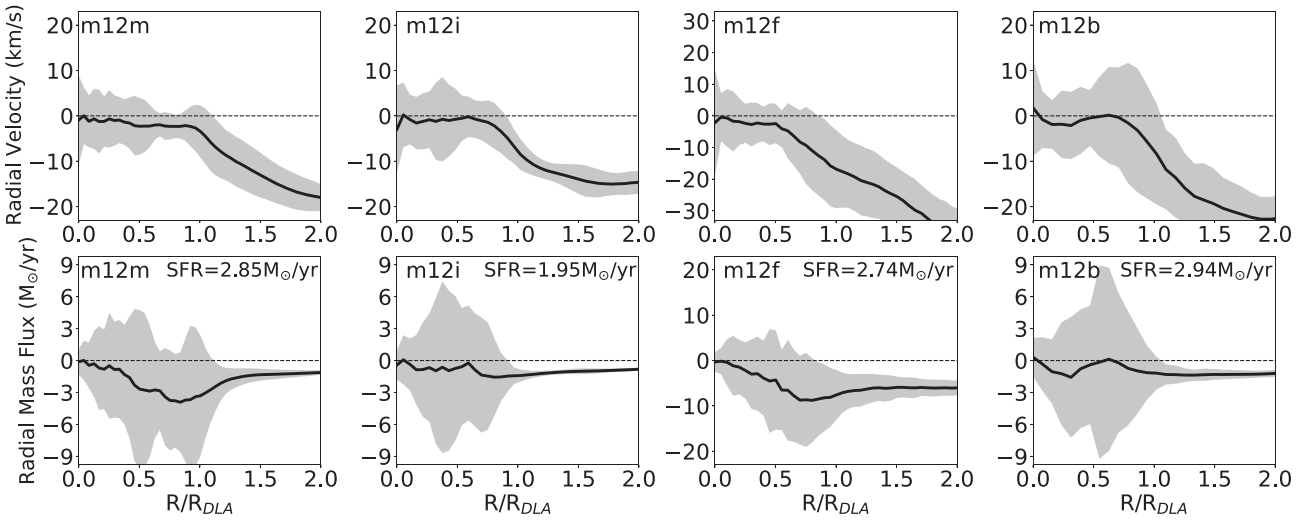


**Figure 4.** Cylindrical radial velocity and mass flux as a function of cylindrical radius measured in 1 kpc radial bins and averaged over 1 $t_{\rm orbit}$ (Table 1). Values were averaged between +/− 10 kpc from the disc plane. Changing this height cutoff has minimal effects on the curves within the disc, but smaller cutoffs significantly reduce the mass flux curve outside the disc. The shaded regions represent the standard deviation of values over time. Bin-averaged radial velocity is $\sim$10 km s$^{-1}$ outside of the disc, but drops to low values within the disc, except in the very centre, which shows higher velocities in some galaxies. Radial mass flux increases going inwards toward the disc, peaking slightly interior to the disc edge, although **m12b** deviates from this trend, largely due to it's smaller disc size and more centrally concentrated star formation. This peak flux is typically of the order of galactic SFR (shown in top right-hand corner for reference), except in **m12f** where a recent merger is driving a strong increase in gas accretion.

**Table 2.** Comparison between total accretion, mass flux through the disc, and SFR within the disc, averaged from redshift z = 0.1 to 0. Total accretion was calculated from the spherical radial mass flux through a 1 kpc spherical shell at 1.5 $R_{\rm DLA}$ (Table 1). Disc mass flux was calculated from the cylindrical radial mass flux through a cylindrical shell at 0.5 $R_{\rm DLA}$ and limited to 2 times the disc scale height. SFR was calculated from the total SFR interior to 1.5 $R_{\rm DLA}$.

| Galaxy | Total accretion ($M_\odot$ yr$^{-1}$) | Disc mass flux ($M_\odot$ yr$^{-1}$) | SFR ($M_\odot$ yr$^{-1}$) |
|---|---|---|---|
| **m12m** | 1.7 ± 0.5 | 2.7 ± 0.4 | 2.5 ± 0.6 |
| **m12i** | 2.2 ± 1.0 | 1.5 ± 0.3 | 1.7 ± 1.5 |
| **m12f** | 3.7 ± 10.3 | 4.4 ± 1.6 | 2.3 ± 2.0 |
| **m12b** | 2.9 ± 1.9 | 1.8 ± 0.7 | 1.9 ± 1.3 |

variation. Fig. 4 quantifies the cylindrical radial velocity and radial mass flux as a function of radius. Within the disc, average radial velocities are on the order of a few km s$^{-1}$. Within 100 Myr of z = 0, the average radial velocities through the disc from **m12m**, **m12i**, **m12f**, and **m12b** are −1.2, −0.4, −4.2, and −1.5 km s$^{-1}$, respectively.

Inflowing gas outside of the disc rapidly slows down by around 10 km s$^{-1}$ as it interacts with disc material. The shaded regions in Fig. 4 show the standard deviation over the time period analysed. The spikes correspond to the pattern of inflow and outflow seen in Fig. 3 and are likely related to spiral arm-like structure.

The radial mass flux curve peaks slightly interior to the shift in radial velocity, possibly by momentum transfer from the infalling gas that joins the disc. Mass flux values decrease gradually with radius outside the disc, and rapidly approach zero towards the centre of the disc as particles become locked up in stars and some are removed out of the disc in a wind/fountain, typically in the vertical direction (Chan, Kereš & Hopkins prep). On average, there is still net radial inflow at all radii, fuelling disc growth.

### 4.2 Angular momentum

Fig. 5 shows specific angular momentum of gas ($\vec{j}$) as a function of galactocentric distance. Within the disc, this curve follows the rotation curve of the galaxy predicted by the enclosed mass very closely.[7] For r ≤ $R_{\rm DLA}$, the specific angular momentum increases with radius roughly linearly as expected for a flat rotation curve. The magnitude of $\vec{j}$ flattens at r > $R_{\rm DLA}$ with only a slight increase with radius as it falls below the value needed for rotational support (Fig. 5, top). Note that gas in the inner CGM still has significantly higher specific angular momentum than the gas within the disc on average, consistent with $|\vec{j}|$ trends found in the CGM of FIRE galaxies in El-Badry et al. (2018). The spread of $|\vec{j}|$ outside the disc increases in all four galaxies. The average $|\vec{j}|$ of gas accreting within 2 $t_{\rm orbit}$ (blue dashed line in Fig. 5) is slightly lower than the overall gas average, especially at larger radii.[8]

While the gas at $r > R_{\rm DLA}$ is not fully rotationally supported, its motion is still strongly aligned with the rotation of the galaxy. The spread in the angular momentum alignment increases for $r > R_{\rm DLA}$ (Fig. 5, bottom). Accreting particles are on average well aligned with the disc but slightly less so than the general inner CGM. A larger degree of misalignment in the central regions is caused by a small fraction of particles that accrete at larger angles, while most join the disc at small angles in the outskirts (Section 4.3).

Individual gas mass elements accrete on to a galaxy while approximately conserving angular momentum from 2–3 $R_{\rm DLA}$ until they reach corotation with the galaxy at $\lesssim R_{\rm DLA}$. In detail, they do lose a small amount of angular momentum as they accrete but these losses are very small, with d$j$/d$r$ ∼ 10–30 kpc km s$^{-1}$ kpc$^{-1}$ on

[7] We use mass enclosed in a sphere of a given radius and for simplicity assume spherical mass distribution when calculating $v_c$, which is sufficiently accurate for our analysis here.

[8] Note that here we mark a gas particle as accreted if it passes within 2 scale heights of the disc (see Section 4.3).

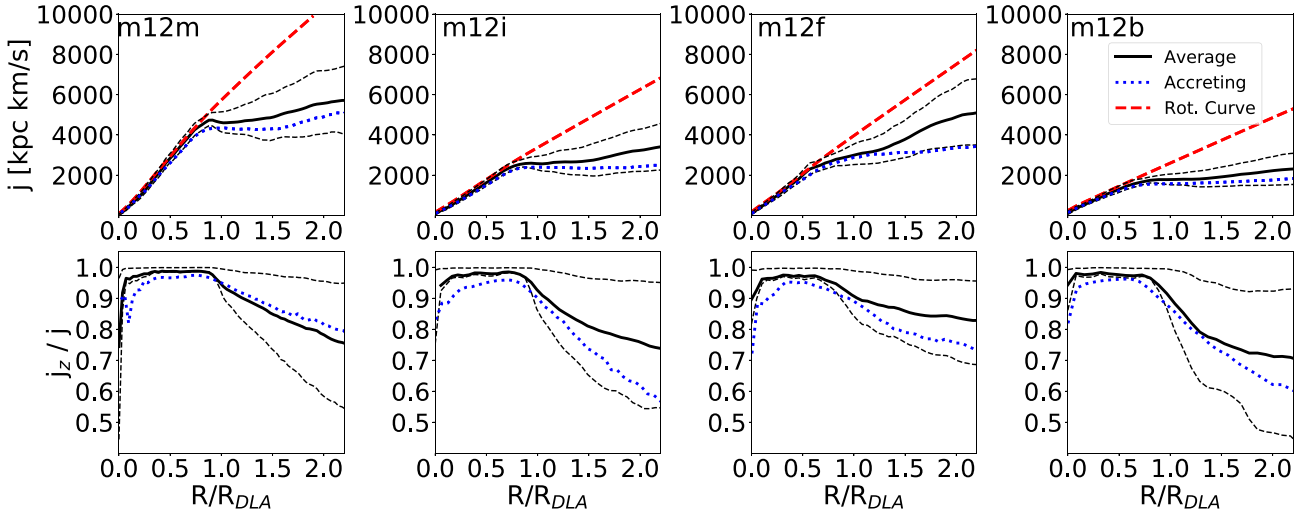


**Figure 5.** Top row: Specific angular momentum as a function of distance from galactic centre at z = 0. The thick-dashed red line represents the expected rotation curve inferred from the mass distribution. The black dashed lines show the standard deviations. The blue dashed lines are the mass-weighted average specific angular momenta of gas elements from the sample of accreting particles described in Section 3.2 1 $t_{\rm orbit}$ prior to accretion. Note that $j$ increases very slowly with radius in the CGM (beyond $R_{\rm DLA}$), and remains only slightly elevated from $j$ at the disc edge. Bottom row: Average z-component of $\vec{j}$ normalized to the total specific angular momentum of each particle. This is a metric of how well particles' rotation is aligned with the disc. More compact discs (e.g. **m12i**, **m12b**) show a sharper drop off at the disc edge, though all gas is still strongly corotating at these scales. Graphs are generated with radial bin resolution of 1 kpc.

average (slightly higher in **m12f**). This is similar to what is shown in Danovich et al. (2012, 2015), which shows that for high-z galaxies, inflowing gas in the halo does not lose a significant amount of angular momentum until it is near the disc.

The specific angular momentum of the gas outside the disc has an effect on where it will reach full rotational support. Gas with $j > j_{\rm disc\text{-}edge}$ will lose the small excess specific angular and settle near the disc edge. Gas with $j < j_{\rm disc\text{-}edge}$ will typically still lose a small amount of angular momentum and enter corotation at a more interior radius.[9] Once within the disc, gas tends to follow the rotation curve closely. During slow radial flow inward gas remains in corotation, resulting in average specific angular momentum loss d$j$/d$r \sim 200$ kpc km s$^{-1}$ kpc$^{-1}$.

### 4.3 Joining the disc

In Fig. 6, we quantify the radius at which gas joins the disc based on where particles enter 1 or 2 times the scale-height of the disc and remain for 1 $t_{\rm orbit}$, as well as where their specific angular momentum reaches within 20 per cent of the rotation curve and remain for 1 $t_{\rm orbit}$ (Section 3.2). Particles tend to enter corotation with the disc at roughly the same radii at which they join the disc geometrically, although there are differences between galaxies. Particles predominantly join the disc within a few kpc of the disc edge ($R_{\rm DLA}$), which is close to $R_{\rm DLA}$ for **m12m** and **m12i**, but closer to 0.5$R_{\rm DLA}$ for the more compact disc in **m12b**. When looking at the medians of the distributions, most particles join the disc outside of 0.5 $R_{\rm DLA}$, with the exception of the 1 scale-height definition for **m12b**. We note that **m12b** is an interesting case compared to the larger, more well-defined discs, showing gas accreting more orthogonally, joining closer to the centre, and showing more centrally concentrated star formation. Relaxing the time criteria pushes this distribution to

[9]In rare cases, accreting gas mass element can have abnormally high specific angular momentum and can lose angular momentum at a rate up to 200 kpc km s$^{-1}$ kpc$^{-1}$ as it is torqued into corotation.

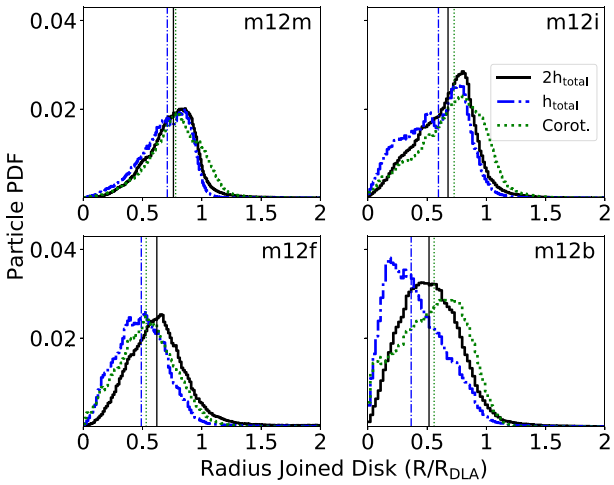


**Figure 6.** Radius at which a particle (from the population tracked from z = 0.2 to z = 0) joins the galactic disc and remains for at least $t_{\rm orbit}$ (Table 1). The black (blue dashed) histogram shows where particles pass 2 scale heights (1 scale height) of the disc. The green dotted histogram shows particle's radial position when its specific angular momentum is within 20 per cent of the value needed for rotational support and remains such for 1 $t_{\rm orbit}$. Histograms are weighted by accreted gas mass. The vertical lines show median values. Particles preferentially join the disc slightly interior to the disc edge ($R_{\rm DLA}$, Table 1), with most particles joining outside of 0.5 $R_{\rm DLA}$. See Fig. B1 for accretion per unit area.

larger radii, slightly closer to the disc edge. In all cases this is well outside of the bulk of the stellar component of the galaxy, typically at $\sim 3 \times R_{*,1/2}$. Our default criteria for when/where a mass element joins the disc will be the geometric classification at two scale heights (black, solid histogram).

Note that when expressed as accretion rate per unit area (see Fig. B1), these distributions tend to be flatter and are in broad agreement semianalytic models of galactic disc evolution that require such flat distributions to match a broad range of disc scaling relations

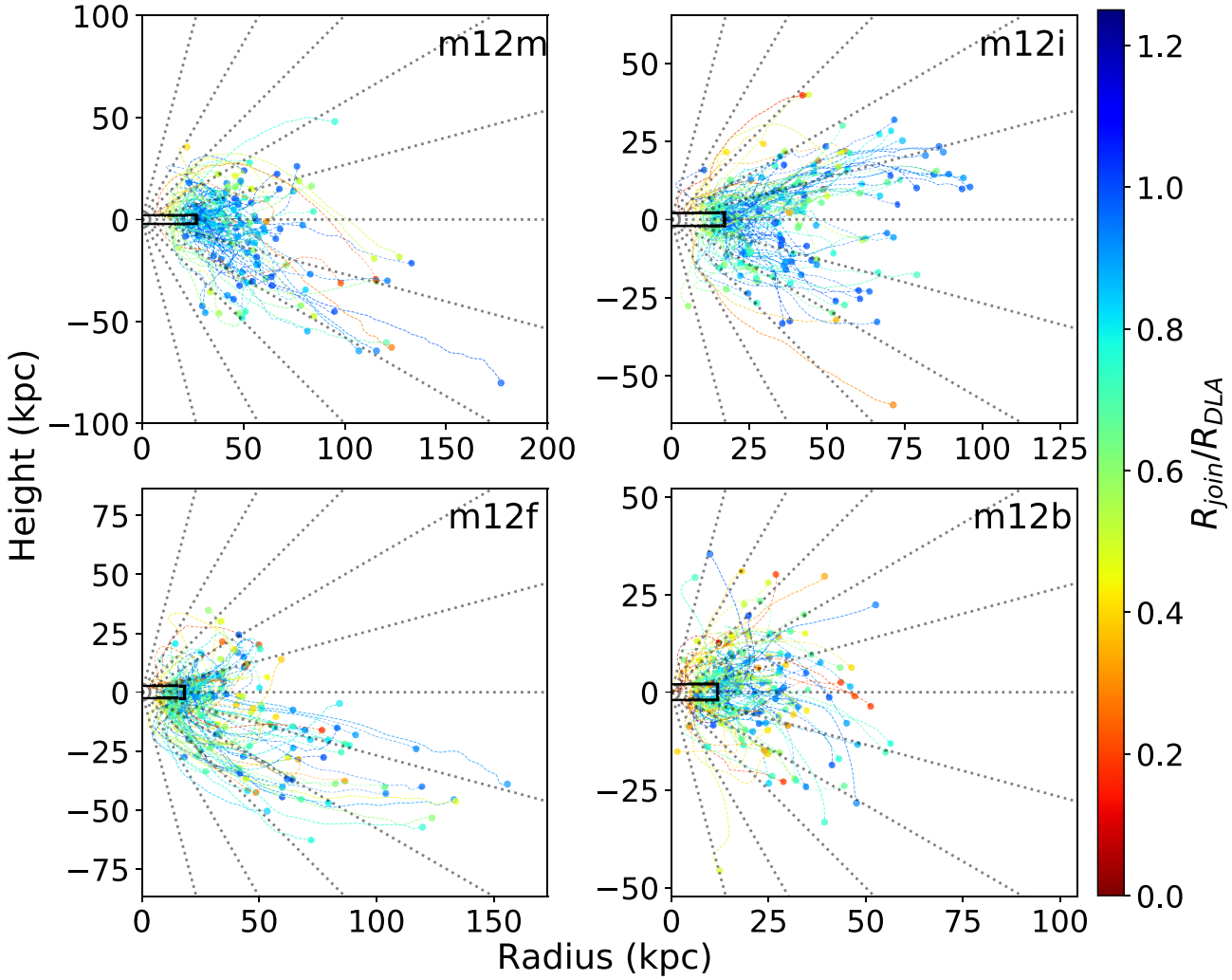


**Figure 7.** Lines visualizing the trajectories for a set of 250 randomly sampled particles from the distribution in Fig. 8. The galactic disc is visualized by the solid black lines representing extent of $R_{\rm DLA}$ and thickness of $\pm h_{\rm total}$. The dashed grey lines show increments of 15°. Trajectories are shown from when the gas elements join the disc to 1.5 $t_{\rm orbit}$ for visualization purposes. Lines are colour coded by the radius at which they join (redder lines correspond to particles that join more interior, colourscale saturates at 1.25 times the radius of the disc). Particles that join more interior tend to have trajectories at higher polar angles. Funnel structure is clearly visible for accreting particles.

(Forbes et al. 2019). However, in the most extended disc in our sample (**m12m**), even the accretion per area is clearly peaked near the disc edge.

Figs 7 and 8 characterize the trajectories individual particles undergo as they accrete on to the disc. As seen in Fig. 7, during accretion particles tend to move parallel to the galactic plane at large distances, before falling on to the disc. The average polar angle (as measured from the centre of the galaxy) of this accretion process is therefore non-zero but small (Fig. 8), with typical values around 15° as measured from galactic centre. This corresponds to flare or funnel-like structures near the disc edge. The angle at which these particles accrete is correlated with where they end up joining the disc. Particles accreting at higher polar angles tend to join the disc at smaller radii.

The angle of these trajectories tends to steepen over time, resulting in larger angles of approach near the location where gas joins the disc. Particles approaching at higher angles ultimately 'fall' on to the disc just prior to joining, showing larger vertical velocities. This effect is still present on average in particles joining closer to the edge, but is much milder. The overall trajectories of accreting gas prior to and after they join the disc are still predominantly parallel to the disc. We emphasize that Fig. 8 shows the mean angle over a single $t_{\rm orbit}$, which will be smaller, on average, than the angle just prior to accretion event. In addition, gas accreting near the plane of the disc tends to have lower radial velocities. In Fig. 7, these particles will be more clustered near the disc edge, making it difficult to distinguish individual trajectories and enabling gas at larger angles to have relatively stronger visual impression in this figure.

To show our selection of accreting particles in Figs 7 and 8 roughly corresponds to what is seen in the total mass flux, we look at the polar angle in terms of radial mass flux of all gas binned in a 1 kpc spherical shell at 1 $R_{\rm DLA}$. We find that the average angle is slightly smaller (∼8°), but is still small and non-zero (Fig. 9).

### 4.4 Directional rates

On galactic scales, gas accretes into star forming regions largely parallel to the disc plane, as opposed to vertically. Fig. 10 shows that the time-averaged vertical mass flux is around an order of magnitude

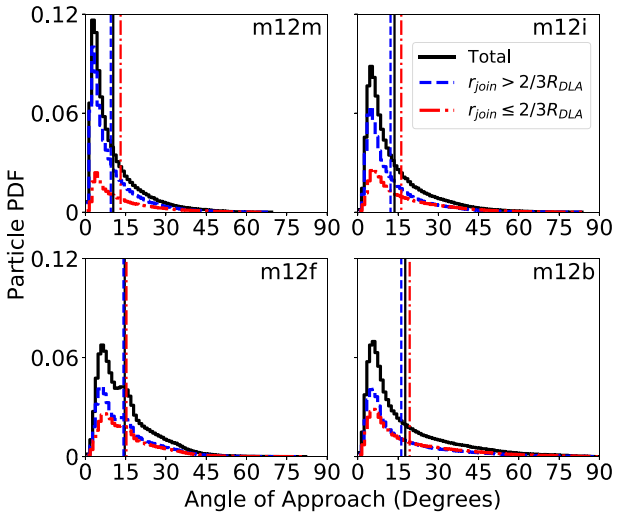


**Figure 8.** Angle above/below the disc plane with which particles accrete on the galaxy, i.e. pass within twice the scale height of the disc and remain for at least 1 $t_{\rm orbit}$. Angle is averaged over the trajectory of the particle for 1 $t_{\rm orbit}$ prior to joining the disc and is measured from galactic centre. The centroid of each distribution is displayed as the vertical dashed line. Colours of the histograms are based on where the particles join the disc. Most particles join the disc at non-zero angles within 15°. Particles that join the disc more centrally tend to accrete at larger angles.

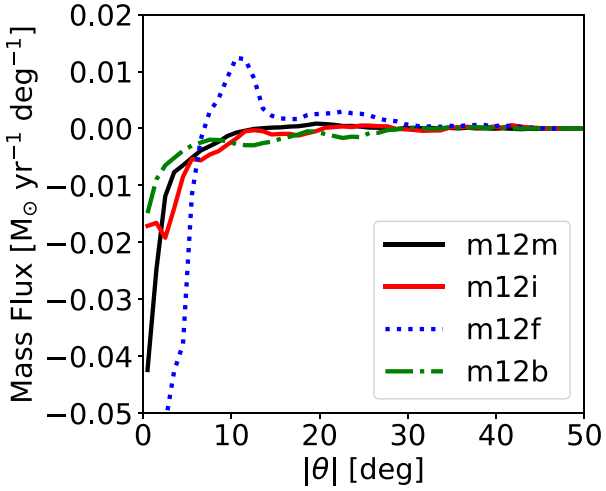


**Figure 9.** Radial mass flux per degree (averaged over 1 $t_{\rm orbit}$) as a function of angle above/below the disc plane. Average angle of inflow is around 8°. Mass flux was calculated through a 1 kpc spherical radial bin centred at 1 $R_{\rm DLA}$ with 2° polar angle bins. Note that **m12f** shows outflowing gas at larger angles owing to the recent merger event.

lower than the parallel component. Galaxies change between periods of net vertical inflow and outflow, while net radial mass fluxes are consistently inflowing. Vertical inflow can still be significant for some short time periods. For instance, the merger event in **m12f** leads to a period where vertical inflow is as almost as significant as radial inflow at redshift 0. We note that parallel infall in Fig. 10 measured at 0.5 $R_{\rm DLA}$ is largely from the gas corotating in the outer disc that moves radially inward as the accretion from the CGM has largely settled into the disc further out. If we constrain our measure of vertical flows to the innermost regions of the galaxy only, we see more consistent vertical outflows. These features ultimately arise

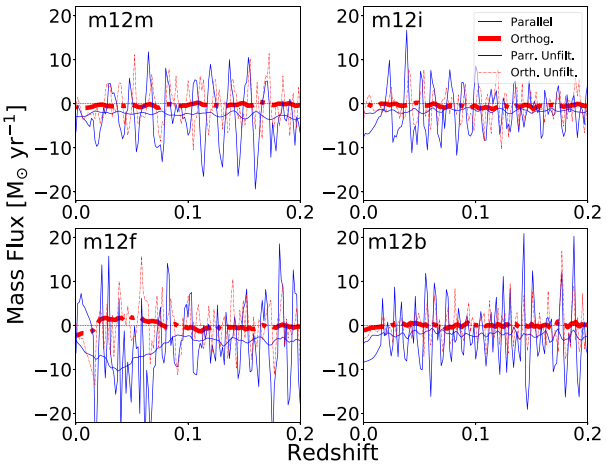


**Figure 10.** Mass fluxes within the disc. The blue, solid lines show mass fluxes parallel to the disc. The red, dashed lines show mass fluxes orthogonal to galactic discs. Negative values represent in-flowing material. Parallel mass fluxes (blue) are measured within 1 scale height of the disc through a 0.5 kpc radial bin centred at 0.5 $R_{\rm DLA}$. Orthogonal mass fluxes are measured within 0.5 $R_{\rm DLA}$ in a 0.5 kpc vertical bin at 1 scale height above the disc. Both scale heights and $R_{\rm DLA}$ were calculated at each time point as described in Table 1 to account for changes in disc size. The thick lines are smoothed using a moving average filter with a window width equal to the dynamical time for each galaxy in order to suppress oscillations. Unfiltered values are shown by thin lines. Note the amplitudes of the smoothed parallel mass fluxes tend to by higher and are consistently inflowing, while the orthogonal mass fluxes show inflow and outflow periods.

from stellar feedback, and typically only have values of 0–0.5 $M_\odot$ yr$^{-1}$.

This trend can be seen on local scales in Figs 3 and B3, which show a colour map corresponding to radial and vertical velocity components, respectively. Gas accretes asymmetrically at the disc edge, with each galaxy showing regions of distinct inward and outward movement with spatial scales of ∼5–20 kpc. This is further visualized in Fig. 11, which shows certain azimuthal angles experiencing strong radial inflows, while others have strong outflows or little net radial flow. Note, Fig. 11 was averaged over a relatively short period of time to emphasize the differences at a given redshift. Dips come from the radial oscillation of gas within and just outside the disc as well as anisotropies of accreting gas at the given time. On average, there is still a radial inflow signature for all galaxies.

Regions of similar size with higher infall or outflow rates are also seen in the vertical mass flux maps for galaxies with stronger vertical flow rates (**m12f**, **m12b**), while the galaxies with weaker flows tend to be less structured and more randomly distributed (**m12m**, **m12i**) (Fig. B3). We do note, however, that we see isolated regions with high vertical velocities, as would be expected from areas with high SFRs that can drive galactic outflows/fountains (see Section 5.4).

### 4.5 Evolution in disc

Fig. 12 characterizes the radial distribution of star formation of each galaxy, showing that the bulk of star formation occurs at radii much smaller than $R_{\rm DLA}$. Given that most particles join the disc near the edge and most of the galactic star formation occurs deeply within the disc (Fig. 12), there must be radial transport through the disc itself in order to sustain this star formation. Although the total star formation is peaked at the centre of the galaxy, as particles transport radially in the disc they form stars at all radii, starting at $R_{\rm DLA}$. Fig. 13 shows a

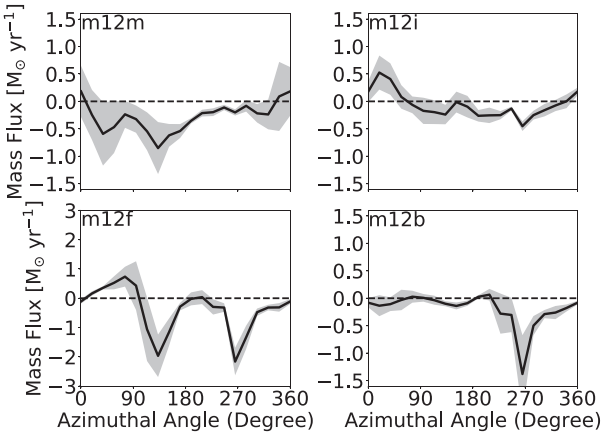


**Figure 11.** Cylindrical radial mass flux through a 1 kpc radial bin at the disc edge ($R_{DLA}$, Table 1) as a function of azimuthal angle on the disc. Data were averaged over 0.25 $t_{orbit}$ near redshift z = 0 for all particles within +/− 2 $h_{disc}$ of the disc plane. Standard deviation over time is shown by the shaded region. Dips in mass flux come largely come from radial oscillations of both the disc material near the edge as well as radial oscillations of the accreting material. Anisotropic distribution of accreting gas also plays a role depending on the galaxy (e.g. the merger event in **m12f**). Figure is averaged over a relatively short period to emphasize angular differences at a given time.

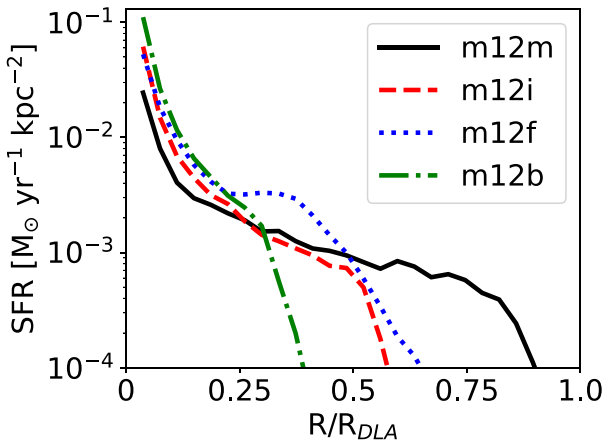


**Figure 12.** Distribution of star formation rate per unit area as a function of cylindrical radius averaged for $0 \leq z \leq 0.2$. SFR per unit area peaks at the centre for all four galaxies. The larger disc galaxies (**m12m**, **m12i**, **m12f**) show star formation at larger radii with a sharp drop off at the disc edge. Star formation in **m12b** is much more centrally peaked.

net radial mass flux rate of around 2 M$_\odot$ yr$^{-1}$ on average within the disc, and how mass flux through the disc drops off as a function of radius as gas is locked up in stars or ejected from the disc. This trend is not clear in **m12b** due to its very centrally concentrated SF.

Our particle tracking analysis shows gas that joins in the outer regions of the disc can eventually transport to more interior star forming regions. The trajectories are not simple, however, with a radial oscillatory component related to spiral arm like structure. Averaging over the gas azimuthally renders this oscillatory motion to a slow overall radial inflow on the order of 1–3 km s$^{-1}$. It is worth noting, that when averaging individual particle trajectories over time, similar velocities are seen (Fig. B2). This implies that the particles that actually fuel star formation in the interior regions can be accreted relatively long ago (i.e. it takes 2 Gyr to travel 10 kpc at 5 km s$^{-1}$).

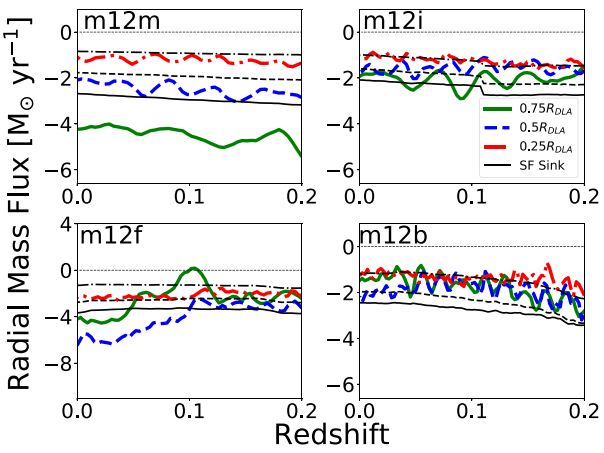


**Figure 13.** Cylindrical radial mass flux through the disc plane. Mass flux was calculated in a 1 kpc radial bin at various radii within the disc, for gas within 2 scale heights of the disc plane. Star formation sink rates (black, thin lines) were calculated as the negative of star formation rate interior to 0.75 $R_{DLA}$, 0.5 $R_{DLA}$, and 0.25 $R_{DLA}$. Both $R_{DLA}$ and the disc scale height were calculated at each time point as described in Table 1 to account for changes in disc size. Curves were smoothed using a moving average with a filter width of 2 dynamical times in order to suppress oscillatory movement. The SFR curve was smoothed as well for consistency, but is relatively stable at late times (Muratov et al. 2015). Mass fluxes closer to the edge for most galaxies are around 2–4 M$_\odot$ yr$^{-1}$, which roughly corresponds to the star formation rate interior to this radius (Table 2). In most galaxies, star formation rates are lower than mass flux through the disc, as some mass is lost in outflows. Mass flux rates drop off as you go further into the galaxy as gas forms stars. Note that **m12f** undergoes a merger event at around redshift 0.1, resulting in heavy accretion and radial transport through the disc.

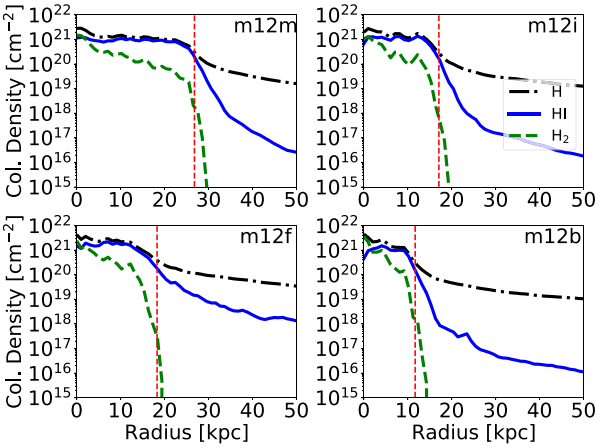


**Figure 14.** Column density as a function of radius for total hydrogen, H I, and $H_2$ for the four galaxies in our sample viewed face on. Vertical dashed lines show $R_{DLA}$. Note, galaxies show a sharp edge signified by a steep drop off in column density. This drop off is less extreme for total hydrogen, as a significant amount is ionized outside the disc.

## 5 DISCUSSION

### 5.1 What determines the disc edge?

Our simulations show gas 'pile-up', i.e. accumulation, at the disc edge, marked by a decrease in average radial speed and ionization, and an increase in column density. In Fig. 14, we show that the change in column density and increase in neutral fraction occur at

a similar radius as the change in radial speed (seen in Fig. 4). This disc radius ($R_{\rm DLA}$) marks a physical 'edge' of the gas distribution, with H I profiles similar to observed inclination-corrected profiles (Ianjamasimanana et al. 2018). Within ±20 per cent of this edge the total projected column density of gas changes by more than an order of magnitude, from less than $10^{20}$ cm$^{-2}$ to $\sim 10^{21}$ cm$^{-2}$. Because of this change, the gas also changes from mostly ionized to mostly neutral. We therefore conclude that the disc 'edge' is caused by a physical accumulation of gas and the ionization change is simply a consequence of the strong density enhancement. Our findings in previous sections provide clear interpretation of this effect: low density, ionized gas accretes at relatively high radial velocities, while exhibiting an overall sense of corotation. As this gas joins the disc edge, it can no longer flow inwards as easily, causing it to slow down in radial direction, on average. This accumulation causes an increase in density and neutral fraction (owing to more efficient self-shielding).

This interpretation of the disc edge marked in H I differs from many previous models, wherein the disc edge is primarily due to ionization change and the disc density structure is implicitly assumed to be much more extended (Corbelli & Salpeter 1993; Schaye 2004; Bland-Hawthorn et al. 2017; Fumagalli et al. 2017). In these models, a break in the H I column density would be expected in the CGM at the photoionization limit ($\sim 5 \times 10^{19}$ cm$^{-2}$). This break was not observed to be a common feature in galaxies in recent observations (Ianjamasimanana et al. 2018), which see a break at higher column densities, similar to our simulations, implying that ionization is not the main factor determining the extent of the H I disc.

This steep drop in the column density of neutral hydrogen with increasing $r$ continues until it reaches column densities of $\sim 10^{17}$ cm$^{-2}$, typically within 1.5–2 $R_{\rm DLA}$. An exception is **m12f**, where a recent merger redistributes the gas, causing a more gradual drop that reaches $N_{\rm H} \sim 10^{18}$ cm$^{-2}$ within about 2 $R_{\rm DLA}$. These sharp drop offs suggest that disc outskirts at $z = 0$ with column densities $\sim 10^{18}-10^{19}$ are not dramatically larger than the extent typically probed by current observations, i.e. $N_{\rm HI} > 10^{19}$ cm$^{-2}$. This has consequences for detectability of lower density H I at $z \sim 0$ from very extended discs by ongoing and future observations (e.g. Pisano, Walter & Stanimirović 2018; Davis & Gross 2019; Pingel 2019; Witherspoon, Wilcots & Masters 2020). Naturally, at higher redshifts, CGM gas has higher characteristic density, enabling more extended intermediate column density gas (Faucher-Giguère et al. 2016). Finally, for rough comparison, we show the approximate column density of molecular hydrogen, which falls off even more sharply at the disc edge, with column densities falling from $10^{20}$ cm$^{-2}$ to less than $10^{15}$ cm$^{-2}$ within 30 per cent of $R_{\rm DLA}$.

### 5.2 Accretion from HVCs and IVCs

In order to roughly estimate accretion from gas within HVCs and IVCs kinematics in our simulations, we calculate their mass flux through a cylindrical surface with a radius of $R_{\rm DLA}$ and a height of ±10 kpc (Fig. 15). We flag HVCs as any particle with deviations from the galactic rotation curve[10] above 70 km s$^{-1}$. IVCs are identified as particles with deviations of 40–70 km s$^{-1}$. In the non-merging large discs, **m12m** and **m12i**, HVC mass fluxes range from 0 to 20 per cent ($\sim$0–1.5 M$_\odot$ yr$^{-1}$) of net accretion and 5–30 per cent ($\sim$0.5–3 M$_\odot$ yr$^{-1}$) of the gas infall rate.[11] The fraction of net mass flux in HVCs is decreasing with time and is negligible at $z \sim 0$. IVC mass fluxes make up a similar percentage of accretion on average, but do not change as significantly with redshift. In **m12f**, a recent merger, there is little HVC or IVC accretion; instead this galaxy shows net HVC outflow. However in a more compact disc, **m12b**, HVC and IVC have similar contributions and jointly dominate the gas infall rate. Particles flagged as HVCs tend to have very low specific angular momenta (order $\vec{j} < \sim 1000$ kpc km s$^{-1}$) and rotate well below the rotation curve at their position.

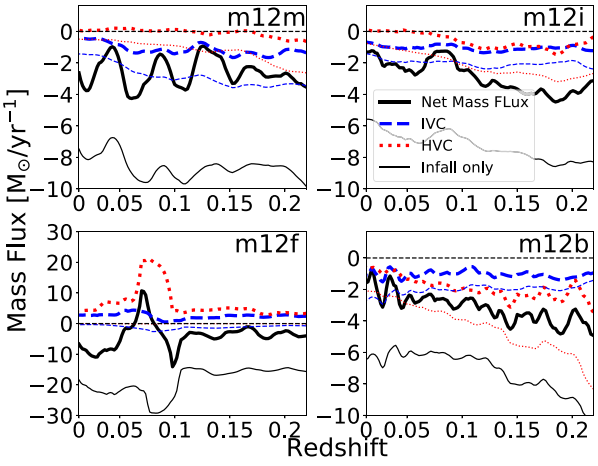


**Figure 15.** Gas mass flux (all gas, from HVCs only, and from IVCs only) through a cylindrical shell with a radius of $R_{\rm DLA}$ and a height of ±10 kpc. Negative values correspond to inflow. The thick lines shows the net mass flux from all gas, while the thin lines show only the mass flux from gas moving radially inward. HVCs and IVCs particles are identified by the deviation from galactic rotation curve as predicted from the enclosed mass as a function of cylindrical radial position. The cutoff for HVCs is above 70 km s$^{-1}$. The cutoff for IVCs is from 40 to 70 km s$^{-1}$. This classification was done in order to approximate observations, however, it does not reflect what would actually be observed from within the galaxies. Instead, it serves as an estimate of the relative contributions of non-corotating gas.

We generally find that HVC mass flux makes up 0−30 per cent of the gas infall rate and of the net gas mass flux rate (net flux contribution is slightly higher in **m12b**) at $z \sim 0$. This implies that most accreting gas is not in HVCs, even when total (ionized+neutral) gas is taken into account, as we do in our analysis. This finding is in rough agreement with observational results of Putman et al. (2012) who found HVCs (total mass of all phases) account for roughly 13–20 per cent of accretion needed given the observed star formation rates. IVCs make up a similar, but slightly higher, fraction of the mass fluxes. Röhser et al. (2016) found IVC accretion rates of 0.52 M$_\odot$ yr$^{-1}$ which is of a similar order as our results. The authors note, however, that they were limited to latitudes above 20° and would expect more IVC accretion from an all sky survey.

This analysis is only a crude estimate of the relative contribution of HVCs and IVCs to the galactic gas accretion at late times and is not perfectly analogous to what would be seen in observations. One important difference is that these values correspond to total gas mass flux, as opposed to neutral hydrogen mass flux (which can be an order

[10] We calculate the deviation of the circular velocity predicted by the enclosed mass interior to the particle's cylindrical radius on the disc and the tangential component of the particle velocity projected on to the disc plane.

[11] Ratios were calculated simply as net mass flux from HVCs only divided by net mass flux of all gas.

of magnitude smaller). Additionally, we are simply counting mass flux through a cylindrical shell at the disc edge. If we track mass flux further out, the proportion of HVC flux increases as gas at larger radii begins to deviate from the rotation of the disc (see Fig. 5), but at the same time, gas neutral fraction drops. Finally, when looking at accretion only (thin lines in Fig. 15), the relative proportions between HVCs, IVCs, and total accretion are similar, but values are higher as outflowing gas has similar kinematics.

An additional caveat of our simple analysis is that we only measure global rates: local deviations that would be seen by an observer within the galaxy could be substantial. For example, different azimuthal angles in Fig. 11 show varying magnitudes of inflow and outflow that will also affect local population of IVCs and HVCs.

Similarly, one would need to know full 3D kinematic information to robustly determine the gas infall rates. While velocities of the approaching gas are broadly aligned with the disc plane, this alignment is not perfect. Figs 7 and 8 show the distribution of polar angles at which gas approaches the disc. These particles typically approach at a small non-zero angle ($\sim$15°). There are few particles approaching the galaxies along the disc plane, and essentially no gas is approaching directly perpendicular to the disc. Interestingly, gas coming in at higher angles ($\theta > \sim$30°) tends to have lower specific angular momenta ($\sim$1000 kpc km s$^{-1}$ lower) and tends to join the disc at smaller radii, avoiding the pile-up of gas at the disc edge (Section 5.1). These particles are more likely to correspond to HVCs and IVCs.

Taking into account full comparison with observations from the perspective within the disc is beyond the scope of this paper and is planned for the future work. Furthermore, we also plan to do a direct comparison with constraints from extraplanar gas kinematics in external galaxies that suggest more significant contribution from vertical gas infall (e.g. Marasco et al. 2019).

### 5.3 Radial mass flux and star formation in disc

As discussed in Section 5.1, as gas joins the disc at large radii, the radial speed slows down to $\sim$1 km s$^{-1}$ on average. The local motion of the gas in the disc is influenced by oscillatory effects from the spiral arms, as well as stellar feedback and to a lesser extent gravitationally powered turbulence (Orr et al. 2020). However, ring averaged net radial motion is inward, producing a net radial transport through the disc of 1–3 km s$^{-1}$ and flow rates comparable to the disc star formation rates ($\sim 2-4$ M$_\odot$ yr$^{-1}$) as shown in Figs 13 and B2.

The alternating velocity structure and related density enhancements show the presence of spiral arm like structure in the four galaxies in our sample. The structure in **m12m**, **m12i**, and **m12f** is floculent in nature, while **m12b** shows more distinct arms. While these oscillations complicate the radial transport of gas through the disc, it has been shown that spiral structure and density inhomogeneities can transport angular momentum to outer Linblad resonances (Lynden–Bell 1979) on galactic scales. On smaller scales, Hopkins & Quataert (2010, 2011) showed that $m = 1$ density inhomogeneities (single armed sprials) can drive gas inflow up to 10 M$_\odot$ yr$^{-1}$ on to central AGNs.

The net accretion rate, SFR, and mass flux through the disc at large radii ($\sim$0.75 $R_{\rm DLA}$) are similar when averaged over time (Table 2), implying a balance between gas inflow and star formation rate. It is worth noting that while the above is true for the net accretion, the total gas infall rates are significantly higher (see Fig. 15) because of outflowing gas component caused by the oscillatory motion and CR-driven outflows from galaxies (Hopkins et al. 2021a; Chan et al. 2021). Goldbaum, Krumholz & Forbes (2015, 2016) similarly studied radial mass fluxes in simulations of galactic discs with and without stellar feedback. In their fiducial runs with stellar feedback, they found mass fluxes on the order of 0.5–1 M$_\odot$ yr$^{-1}$with SFRs of 2–3 M$_\odot$ yr$^{-1}$. Unlike this study, these simulations were non-cosmological and looked at discs in earlier stages, before equilibrium is reached. When equilibrium is reached, the SFR may more closely match the radial mass flux at all radii, as we see in our study.

As gas transports inwards it becomes locked up in stars, resulting in the overall mass flux rate dropping with decreasing radius. This can be seen clearly in Figs 4 and 13. In general, infall rate can be slightly higher than star formation rate owing to galactic outflows that can eject some of the gas supplied to the disc. Depending on the distribution of star formation in each galaxy (Fig. 12), we expect to see differences in how this drop off behaves as a function of radius. While in all galaxies the star formation per unit area peaks at small radii, the total star formation in **m12m** is more evenly distributed throughout the disc. Consequently, in Fig. 13 we see roughly constant drop in mass flux between radii, reaching a much smaller value at the smallest radius. Alternatively, **m12i** shows a stronger peak of star formation in central region, resulting in a smaller change between the inner and outer radii on average. In a more extreme case, **m12b** has almost all star formation in the centre-most region due to its small disc size. Correspondingly, the mass fluxes through the entire disc are roughly equivalent, only decreasing slightly on average.

While average radial infall speeds seen in azimuthal rings or time averaged gas motion are low (see Figs 4, 13), the process of radial infall still requires slow, but continuous net angular momentum loss. We will explore the physics of this process in future work. Additionally, it is worth noting that our average inflow velocities are broadly consistent with what is predicted by theoretical models of 'gravitoturbulent' discs or discs with an effective 'turbulent viscosity' (Gammie 2001; Rice, Lodato & Armitage 2005; Cossins, Lodato & Clarke 2009; Hopkins & Christiansen 2013), which (for supersonic, isotropic turbulence) predict inflow rates $\dot{M} \sim 2\pi\,\sigma_{\rm turb}^2\,\Sigma_{\rm gas}/\Omega$ (Thompson, Quataert & Murray 2005), or net radial inflow velocities $\langle v_r \rangle \sim (\sigma_{\rm turb}/V_c)\,\sigma_{\rm turb}$. For a velocity dispersion here of $\sigma_{\rm turb} \sim 10-25$ km s$^{-1}$ (Chan et al., in preparation) and circular velocity $V_c \sim 200$ km s$^{-1}$ predicts $\langle v_r \rangle \sim 0.5-3$ km s$^{-1}$. This suggests a steady, 'gravitoturbulent' effective angular momentum loss rate on large scales may be a reasonable approximation.

### 5.4 Additional observational implications

In this section, we comment on the viability of observing accretion near the disc edge in cases of more stable discs (**m12m** and **m12i**) and discs with heavier accretion (**m12f** and **m12b**), as well as radial gas flows within the disc. H I column densities remain above $10^{19}$ cm$^{-2}$ during the transition between the relatively uniform, moderate velocity flow close to the disc edge and much lower average radial velocities inside the disc (Fig. 14), making such a transition readily observable in H I emission as well as absorption in H I and associated metal species.

Outside the disc in more stable galaxies (**m12m** and **m12i**), we expect to see inflow velocities peaking around 30–40 km s$^{-1}$ with infalling region length scales of 1–10 kpc (Fig. 11). We predict a ring averaged inflow velocity for this region of around 10 km s$^{-1}$. Werk et al. (2019) and Bish et al. (2019) have mapped absorption signatures toward a sample of seven blue horizontal branch stars above the Milky Way's disc using data from the Cosmic Origins

Spectrograph (COS; Froning & Green 2009) and Keck/HIRES (Vogt et al. 1994). They found coherent ionized structures at the disc–halo interface with scale lengths of at least 1 kpc and radial velocities of 30–50 km s$^{-1}$, which is comparable to our expectations. Given the survey geometry (looking for absorption above the disc not far from the Solar circle), it is likely that the dominant gas accretion component would be missed by such a survey. As shown in Fig. 7 and Fig. 8, the average angle of approach is small. We note, however, that gas approaching at higher angles tends to increase the angle at which it joins the disc (i.e. falls on to the disc) just prior to joining. The local angle of accretion for this gas would therefore be higher than these figures may imply. In future work, we plan to do a more detailed comparison with from the Solar circle perspective in our simulated galaxies.

Ho & Martin (2020) used Mg II absorbers from background quasars near z = 0.2 galaxies (Ho et al. 2017; Martin et al. 2019) coupled with galaxy orientation based on high resolution images to constrain maximum radial inflow speeds to 30–40 km s$^{-1}$ along two lines of sight in separate galaxies (at galactocentric radii of 69 and 115 kpc). However, along other lines of sight, they are not able to successfully model radial inflow in agreement with their constraints on disc orientation, leading the authors to conclude there is no radial inflow. While their sightlines probe further from the galaxies than the region of focus in this work, these results are in agreement with both our numerical values for inflow velocities, as well as anisotropic accretion around the simulated disc galaxies, with some regions having no inflow at a given time.

For galaxies undergoing more active accretion (**m12b** and **m12f**), we predict a peak inflow rate as high as 50 and 100 km s$^{-1}$ respectively, with ring averaged velocities around 15 km s$^{-1}$. Zheng et al. (2017) observed seven UV bright disc stars in M33 as background sources using the COS in order to identify significant ionized gas accretion. Accretion velocity was $v_{\rm acc} = 100^{+15}_{-20}$ km s$^{-1}$ and estimated mass flux was 2.9 M$_\odot$ yr$^{-1}$ (5.8 M$_\odot$ yr$^{-1}$ if flows are axisymmetric). While these are within the range of values for our simulated MW-mass galaxies, M33 has significantly lower mass and is therefore expected to have lower (long-term averaged) infall rate. The authors note that this high mass flux rate is likely transient, either due to reaccretion from a large galactic fountain event, or recent interaction with M31. Note that total infall rates are higher than net accretion rates owing to infall/outflow variations in and around the disc. Extrapolation of individual regions into disc averaged quantities is therefore very uncertain.

Within the disc, local gas motion (infall and outflowing gas) can be strongly affected by the oscillations caused by the spiral arms, as well as local feedback and collapse, often driving the gas up to 30–40 km s$^{-1}$. However, when ring averaged, our simulations predict radial gas inflow on the order of 1–3 km s$^{-1}$ (see Figs 4 and B2). The difficulty of determining radial velocities from a single orientation complicates observation of these flows. If galaxies are viewed perfectly face-on, radial velocities would be impossible to detect. If viewed perfectly edge on, it would be difficult to spatially resolve different regions in the disc so additional modelling of the observed gas velocities is needed.

Wong et al. (2004) searched for radial flow signatures within the disc using CO and H I velocity fields in seven nearby spirals by decomposing the velocity fields of concentric elliptical rings into a third-order Fourier series. For three galaxies, an upper limit of 5–10 km s$^{-1}$ for inflow velocities were determined. These limits are consistent with our ring averaged inflow velocities (Fig. 4). For our simulated galaxies ring averaged velocities within 0–0.5$R_{\rm DLA}$ are very small, 1–3 km s$^{-1}$ depending on the ring and galaxy, while values can be larger in the outskirts.[12]

A similar study using 10 galaxies from the THINGS survey with stellar masses comparable to our sample (Schmidt et al. 2016) found radial inflows signatures as a function of radius for a few of these galaxies. Inside the optical radius for certain galaxies, the authors found ring-averaged radial inflow velocities on the order of ∼5–20 km s$^{-1}$ with corresponding mass fluxes of ∼0.1–4.0 M$_\odot$ yr$^{-1}$ depending on the radius within each galaxy. This uncertainty range is in general agreement with out findings when time variations in accretion rate and velocity are accounted for. Contrary to what was expected from their simplified model of galaxy formation, the mass fluxes varied strongly as a function of radius, instead of steadily decreasing with radius based on the interior star formation rate. This is likely due to the fact that they are only able to observe a single time point, which will be confounded by spiral structure oscillations and outflow events. As shown in the bottom row of Fig. 4, dispersion over time and radial variations in the mass flux are much larger than average values.

### 5.5 Comparison to simulations without cosmic rays

In this section, we briefly summarize the differences between the simulations used in this study (Hopkins et al. 2020) (CR+), simulations with the same model but omitting CRs, (MHD+), and previous FIRE-2 simulations without MHD and cosmic ray physics (Hydro+) (Hopkins et al. 2018). Further analysis can be found in Appendix A.

The addition of cosmic rays has an effect on the specific quantitative results of our paper, however, the qualitative picture remains roughly the same. The higher infall rates in the Hydro+ and MHD+ runs (Fig. A4) drive a factor of 2–3 higher star formation within the disc A1. Feedback energy and momentum input, as well as gravitationally driven turbulence cause higher disc velocities. Velocity dispersions within the CR+ and Hydro+ runs are 10–25 km s$^{-1}$ and 15–30 km s$^{-1}$, respectively (Gurvich et al. 2020; Orr et al. 2020; Chan et al., in preparation). This can also be seen in the larger flow velocities within the disc in the Hydro+ runs, both in the extrema at a given time point (∼60 km s$^{-1}$) (Fig. A2) and on average (∼5–10 km s$^{-1}$ averaged azimuthally) (Fig. A3).

The interaction between the CRs and gas outside the disc is the primary cause of the above differences. Gas outside the disc in the CR runs tends to be falling in at lower velocities. Additionally, Hopkins et al. (2021a) shows that CR-driven winds are preferentially driven perpendicular to the disc plane, confining infalling gas to closer alignment with the plane. By comparison, the Hydro+ runs tend to have higher infalling velocities in the inner CGM (Fig. A3), and approach the disc plane from larger angles on average (Fig. A6). The dominant inflow is still parallel to the disc on average, however the mass fluxes in the Hydro+ and MHD+ runs vary more strongly over time (Fig. A7). The nature of gas accretion at late times as well as its thermal properties and connection to the cooling flow solution in Hydro+ simulations will be further explored in Hafen et al. (in preparation).

[12]Two galaxies in the Wong et al. (2004) sample also showed signs of radial outflows at 45 and 60 km s$^{-1}$ (with similar uncertainties as the inflow signatures), which match the instantaneous radial velocities seen in Fig. 3. For some galaxies, inclinations were too low or uncertain to be able to identify any radial flows.

While there are observational constraints (specifically gamma-ray emission) for CR transport on galactic scales that were used to select a default value for the constant diffusion coefficient, $\kappa_{||} = 3 \times 10^{29}\,\mathrm{cm^2\,s^{-1}}$, (Chan et al. 2019; Hopkins et al. 2020), there are currently no direct constraints on the CRs in the CGM. The constant diffusion model in our simulations is the simplest possibility, however there are more physically motivated models for CR diffusion and streaming that we have recently tested in Hopkins et al. (2021c). When constrained to match observations on galactic scales, these models result in higher effective diffusion within the CGM, suggesting lower overall CR energy density and pressure gradients. The outcome is that the resulting effects on the CGM, SFRs, and galactic outflows in these models lie in-between our Hydro+ runs and our CR runs with constant diffusion (Hopkins et al. 2021b). We expect similar conclusions to apply for the gas infall. In this respect Hydro+/MHD+ and CR+ runs represent two different limiting cases describing the nature of gas infall on galactic scales.

## 6 CONCLUSIONS

We analyse gas accretion in and around four low redshift $L_*$ disc galaxies simulated using the FIRE-2 model with feedback from cosmic rays. Galaxies span a wide range of disc sizes. We find the dominant source of accretion is gas that is largely corotating and joining near the gaseous disc edge. Galactic gas then radially flows inward towards regions with active star formation with low (time and azimuthally averaged) velocities of few $\mathrm{km\,s^{-1}}$.

The key points of our paper are summarized below:

(i) Net accretion rate on to the galaxy roughly corresponds to radial gas mass flux through the disc and total star formation rate of late time MW mass galaxies.

(ii) Infalling gas within tens of kpc from the disc is moving primarily parallel to the disc. Infalling mass flux in the direction vertical to the disc is subdominant.

(iii) Gas in the inner CGM is largely corotating with the disc with specific angular momentum similar to the disc edge but below value needed for full rotational support. As the gas moves radially and accretes to the disc, it largely conserves angular momentum with only a small loss until it reaches full rotational support, typically just after crossing the gaseous disc edge.

(iv) Because infalling gas largely corotates, the ring averaged infall velocity 30–40 kpc from the centre of the non-interacting MW-mass discs is only $\sim$20 $\mathrm{km\,s^{-1}}$, a small fraction of rotational velocity. Time averaged radial velocities drop to $\sim$10 $\mathrm{km\,s^{-1}}$ for (20–30 $\mathrm{km\,s^{-1}}$ for a disc with recent interaction) at $\sim \mathrm{R_{DLA}}$, radius at which neutral gas column density reaches DLA limit, which we take to be the disc edge. This effect and strong alignment of the gas infall with the disc, make it difficult to observationally quantify gas infall in the inner CGM. Our results suggest future observations of gas around local MW-mass star forming discs galaxies to include corotating gas near the disc when accounting for the galactic gas accretion.

(v) Because the dominant source of accretion is gas that is largely corotating, the gas with HVCs and IVCs velocities is typically a subdominant component.

(vi) Accreting gas tends to 'pile up' at the disc edge. As gas from the CGM joins the disc, its radial speed drops from 10–20 $\mathrm{km\,s^{-1}}$ to 1–3 $\mathrm{km\,s^{-1}}$ and density increases, causing a fast change in its ionization state. This has consequences for the observability of the extended neutral gas structures well outside $R_{\mathrm{DLA}}$.

(vii) Gas accretes at small non-zero angles, typically 5–20° above or below the disc when viewed one orbital period before joining the disc. Gas coming in at larger angles tend to fall on to the disc edge prior to joining, showing larger vertical velocities during the process.

(viii) Most gas joins the disc close but slightly interior to the gaseous disc edge. In all cases this is well outside the bulk of the stellar disc, typically at $\sim 3R_{*,1/2}$.

(ix) Once in the disc, radial movement of the gas is complex. In addition to local disturbance by feedback and collapse, there is larger scale motion likely due to spiral arm like structure. Despite relatively high instantaneous radial velocities (up to $\sim$20–40 $\mathrm{km\,s^{-1}}$), time and azimuthally averaged bulk radial transport has net velocities of only several $\mathrm{km\,s^{-1}}$.

(x) Observations of radial flows within the disc will need to be handled with care, keeping in mind the time and spatial variations that dominate over long-term average trends. Clear signal of the radial gas flow requires $\sim \mathrm{km\,s^{-1}}$ accuracy from large sample of disc galaxies.

(xi) Gas infall in simulations without cosmic rays is qualitatively similar. However, the infall velocities and gas infall rates are on average higher than in simulations with cosmic rays (up to 50 $\mathrm{km\,s^{-1}}$ at distance twice the disc edge and infall rates of $\sim 5\,\mathrm{M_\odot\,yr^{-1}}$), with much higher time variations in both.

In future work, we plan to make more direct comparison of our simulations with observations of the Milky Way and resolved disc galaxies at $z \sim 0$. This will include mock observations of simulated H I emission and absorption spectra of different ions for spatially resolved 'down the barrel' analysis, mock observations from the 'solar circle' perspective, and the analysis of extraplanar gas kinematics.

We will also investigate angular momentum evolution of gas as it accretes and flows within galaxies, including the physical origin of the related angular momentum loss.

We note that most of our findings are qualitatively similar in simulations with and without CRs but quantitative differences in gas velocities and accretion rates can be significant. Difference in gas phase structure are also significant (Ji et al. 2020). We therefore plan to analyse simulations with a broader set of CR transport models that span the range between models with constant diffusion of CRs and Hydro+ (see Section 5.5).

## ACKNOWLEDGEMENTS

DK was supported by National Science Foundation (NSF) grants AST-1715101 and AST-2108314, and the Cottrell Scholar Award from the Research Corporation for Science Advancement. CAFG was supported by NSF through grants AST-1715216 and CAREER award AST-1652522; by the National Aeronautics and Space Administration (NASA) through grant 17-ATP17-0067; and by a Cottrell Scholar Award from the Research Corporation for Science Advancement. Support for PFH was provided by NSF Research Grants 1911233 & 20009234, NSF CAREER grant 1455342, NASA grants 80NSSC18K0562, *HST*-AR-15800.001-A. Numerical calculations were run on the Caltech compute cluster 'Wheeler,' allocations FTA-Hopkins/AST20016 supported by the NSF and the Texas Advanced Computing Center (TACC), and NASA HEC SMD-16-7592. TKC was supported by the Science and Technology Facilities Council (STFC) through Consolidated Grants ST/P000541/1 and ST/T000244/1 for Astronomy at Durham. IE was supported by a Carnegie-Princeton Fellowship through the Carnegie Observatories. AW received support from NSF CAREER grant 2045928; NASA

Astrophysics Theory Program (ATP) grants 80NSSC18K1097 and 80NSSC20K0513; *Hubble Space Telescope (HST)* grants GO-14734, AR-15057, AR-15809, and GO-15902 from Space Telescope Science Institute (STScI); a Scialog Award from the Heising-Simons Foundation; and a Hellman Fellowship. The simulations presented here used computational resources granted by the Extreme Science and Engineering Discovery Environment (XSEDE), which is supported by National Science Foundation (NSF) grant no. OCI-1053575, specifically allocation TG-AST120025 and resources provided by PRAC NSF.1713353 supported by the NSF. This work also made use of MATPLOTLIB (Hunter 2007), NUMPY (van der Walt, Colbert & Varoquaux 2011), SCIPY (Jones 2001), and NASA's Astrophysics Data System. We would like to thank the Kavli Institute for Theoretical Physics, supported in part by the National Science Foundation (NSF) under grant no. NSF PHY-1748958, and the participants of the *Fundamentals of Gaseous Halos* program for interactions that improved this work.

## 7 DATA AVAILABILITY

The data supporting the plots within this article are available on reasonable request to the corresponding author. A public version of the GIZMO code is available at http://www.tapir.caltech.edu/~phopkins/Site/GIZMO.html (Hopkins 2015).

Additional data including simulation snapshots, initial conditions, and derived data products are available at http://fire.northwestern.edu (Hopkins et al. 2018).

## REFERENCES

Anglés-Alcázar D., Faucher-Giguère C.-A., Kereš D., Hopkins P. F., Quataert E., Murray N., 2017, MNRAS, 470, 4698
Barcons X., Lanzettat K. M., Webb J. K., 1995, Nature, 376, 321
Bellardini M. A., Wetzel A., Loebman S. R., Faucher-Giguère C.-A., Ma X., Feldmann R., 2021, MNRAS, 505, 4586
Benincasa S. M. et al., 2020, MNRAS, 497, 3993
Bielby R., Crighton N. H. M., Fumagalli M., Morris S. L., Stott J. P., Tejos N., Cantalupo S., 2017, MNRAS, 468, 1373
Binney J., Dehnen W., Bertelli G., 2000, MNRAS, 318, 658
Bish H. V., Werk J. K., Prochaska J. X., Rubin K. H. R., Zheng Y., O'Meara J. M., Deason A. J., 2019, ApJ, 882, 76
Bland-Hawthorn J., Maloney P. R., Stephens A., Zovaro A., Popping A., 2017, ApJ, 849, 51
Bouché N., Murphy M. T., Kacprzak G. G., Péroux C., Contini T., Martin C. L., Dessauges-Zavadsky M., 2013, Science, 341, 50
Brooks A. M., Governato F., Quinn T., Brook C. B., Wadsley J., 2009, ApJ, 694, 396
Bryan G. L., Norman M. L., 1998, ApJ, 495, 80
Ceverino D., Dekel A., Bournaud F., 2010, MNRAS, 404, 2151
Chan T. K., Keres D., B. Gurvich A., Hopkins P. F., Trapp C., Ji S., Faucher-Giguere C.A., 2021, The impact of cosmic rays on dynamical balance and disk-halo interaction in Lstar disk galaxies, eprint( arXiv:2110.06231)
Chan T. K., Kereš D., Hopkins P. F., Quataert E., Su K. Y., Hayward C. C., Faucher-Giguère C. A., 2019, MNRAS, 488, 3716
Chan T. K., Kereš D., Oñorbe J., Hopkins P. F., Muratov A. L., Faucher-Giguère C.-A., Quataert E., 2015, MNRAS, 454, 2981
Corbelli E., Salpeter E. E., 1993, ApJ, 419, 104
Cossins P., Lodato G., Clarke C. J., 2009, MNRAS, 393, 1157
Danovich M., Dekel A., Hahn O., Ceverino D., Primack J., 2015, MNRAS, 449, 2087
Danovich M., Dekel A., Hahn O., Teyssier R., 2012, MNRAS, 422, 1732
Davis J., Gross J., 2019, American Astronomical Society Meeting Abstracts #233, 363.16
Dekel A., Birnboim Y., 2006, MNRAS, 368, 2
Dekel A., Sari R., Ceverino D., 2009, ApJ, 703, 785
Diamond-Stanic A. M., Coil A. L., Moustakas J., Tremonti C. A., Sell P. H., Mendez A. J., Hickox R. C., Rudnick G. H., 2016, ApJ, 824, 24
El-Badry K. et al., 2018, MNRAS, 473, 1930
Fall S. M., Efstathiou G., 1980, MNRAS, 193, 189
Faucher-Giguère C.-A., Feldmann R., Quataert E., Kereš D., Hopkins P. F., Murray N., 2016, MNRAS, 461, L32
Faucher-Giguère C.-A., Hopkins P. F., Kereš D., Muratov A. L., Quataert E., Murray N., 2015, MNRAS, 449, 987
Faucher-Giguère C.-A., Kereš D., Ma C.-P., 2011, MNRAS, 417, 2982
Faucher-Giguère C.-A., Lidz A., Zaldarriaga M., Hernquist L., 2009, ApJ, 703, 1416
Feldmann R., Hopkins P. F., Quataert E., Faucher-Giguère C.-A., Kereš D., 2016, MNRAS, 458, L14
Forbes J. C., Krumholz M. R., Speagle J. S., 2019, MNRAS, 487, 3581
Froning C. S., Green J. C., 2009, Ap&SS, 320, 181
Fumagalli M., Haardt F., Theuns T., Morris S. L., Cantalupo S., Madau P., Fossati M., 2017, MNRAS, 467, 4802
Gammie C. F., 2001, ApJ, 553, 174
Goldbaum N. J., Krumholz M. R., Forbes J. C., 2015, ApJ, 814, 131
Goldbaum N. J., Krumholz M. R., Forbes J. C., 2016, ApJ, 827, 28
Gurvich A. B. et al., 2020, MNRAS, 498, 3664
Guszejnov D., Grudić M. Y., Offner S. S. R., Boylan-Kolchin M., Faucher-Giguère C.-A., Wetzel A., Benincasa S. M., Loebman S., 2020, MNRAS, 492, 488
Hafen Z. et al., 2017, MNRAS, 469, 2292
Haywood M., Snaith O., Lehnert M. D., Di Matteo P., Khoperskov S., 2019, A&A, 625, A105
Ho S. H., Martin C. L., 2020, ApJ, 888, 14
Ho S. H., Martin C. L., Kacprzak G. G., Churchill C. W., 2017, ApJ, 835, 267
Ho S. H., Martin C. L., Turner M. L., 2019, ApJ, 875, 54
Hopkins P. F. et al., 2018, MNRAS, 480, 800
Hopkins P. F. et al., 2020, MNRAS, 492, 3465
Hopkins P. F., 2015, MNRAS, 450, 53
Hopkins P. F., Chan T. K., Ji S., Hummels C. B., Kereš D., Quataert E., Faucher-Giguère C.-A., 2021a, MNRAS, 501, 3640
Hopkins P. F., Chan T. K., Squire J., Quataert E., Ji S., Kereš D., Faucher-Giguère C.-A., 2021b, MNRAS, 501, 3663
Hopkins P. F., Christiansen J. L., 2013, ApJ, 776, 48
Hopkins P. F., Kereš D., Murray N., Quataert E., Hernquist L., 2012, MNRAS, 427, 968
Hopkins P. F., Kereš D., Oñorbe J., Faucher-Giguère C.-A., Quataert E., Murray N., Bullock J. S., 2014, MNRAS, 445, 581
Hopkins P. F., Quataert E., 2010, MNRAS, 407, 1529
Hopkins P. F., Quataert E., 2011, MNRAS, 415, 1027
Hopkins P. F., Squire J., Chan T. K., Quataert E., Ji S., Kereš D., Faucher-Giguère C.-A., 2021c, MNRAS, 501, 4184
Hopkins P. F., 2015, MNRAS, 450, 53
Hunter J. D., 2007, Comput. Sci. Eng., 9, 90
Ianjamasimanana R., Walter F., de Blok W. J. G., Heald G. H., Brinks E., 2018, AJ, 155, 233
Ji S. et al., 2020, MNRAS, 496, 4221
Jones E., Oliphant T., Peterson, P., 2001, SciPy: Open Source Scientific Tools for Python
Kassin S. A. et al., 2012, ApJ, 758, 106
Kennicutt R. C. Jr, 1998, ApJ, 498, 541
Kereš D., Hernquist L., 2009, ApJ, 700, L1
Kereš D., Katz N., Fardal M., Davé R., Weinberg D. H., 2009, MNRAS, 395, 160
Kereš D., Katz N., Weinberg D. H., Davé R., 2005, MNRAS, 363, 2
Kroupa P., 2001, MNRAS, 322, 231
Krumholz M. R., Burkhart B., Forbes J. C., Crocker R. M., 2018, MNRAS, 477, 2716
Krumholz M. R., Gnedin N. Y., 2011, ApJ, 729, 36
Krumholz M., Burkert A., 2010, ApJ, 724, 895
Lacki B. C., Thompson T. A., Quataert E., Loeb A., Waxman E., 2011, ApJ, 734, 107
Leitherer C. et al., 1999, ApJS, 123, 3

Leitner S. N., Kravtsov A. V., 2011, ApJ, 734, 48
Lynden-Bell D., 1979, MNRAS, 187, 101
Ma X., Hopkins P. F., Faucher-Giguère C.-A., Zolman N., Muratov A. L., Kereš D., Quataert E., 2016, MNRAS, 456, 2140
Ma X., Hopkins P. F., Wetzel A. R., Kirby E. N., Anglés-Alcázar D., Faucher-Giguère C.-A., Kereš D., Quataert E., 2017, MNRAS, 467, 2430
Mandelker N., Dekel A., Ceverino D., Tweed D., Moody C. E., Primack J., 2014, MNRAS, 443, 3675
Marasco A. et al., 2019, A&A, 631, A50
Martin C. L., Ho S. H., Kacprzak G. G., Churchill C. W., 2019, ApJ, 878, 84
Martin C. L., Shapley A. E., Coil A. L., Kornei K. A., Bundy K., Weiner B. J., Noeske K. G., Schiminovich D., 2012, ApJ, 760, 127
Muratov A. L. et al., 2017, MNRAS, 468, 4170
Muratov A. L., Kereš D., Faucher-Giguère C.-A., Hopkins P. F., Quataert E., Murray N., 2015, MNRAS, 454, 2691
Muzahid S., Kacprzak G. G., Charlton J. C., Churchill C. W., 2016, ApJ, 823, 66
Nelson D., Vogelsberger M., Genel S., Sijacki D., Kereš D., Springel V., Hernquist L., 2013, MNRAS, 429, 3353
Ocvirk P., Pichon C., Teyssier R., 2008, MNRAS, 390, 1326
Oklopčić A., Hopkins P. F., Feldmann R., Kereš D., Faucher-Giguère C.-A., Murray N., 2017, MNRAS, 465, 952
Oppenheimer B. D., Davé R., Kereš D., Fardal M., Katz N., Kollmeier J. A., Weinberg D. H., 2010, MNRAS, 406, 2325
Orr M. E. et al., 2018, MNRAS, 478, 3653
Orr M. E. et al., 2020, MNRAS, 496, 1620
Pandya V. et al., 2021, MNRAS, 508, 2979
Péroux C. et al., 2017, MNRAS, 464, 2053
Pingel N., 2019, in A Synoptic View of the Magellanic Clouds: VMC, Gaia and Beyond. ESO, Garching, p. 62
Pisano D., Walter F., Stanimirović S., 2018, in Murphy E. and the ngVLA Science Advisory Council, eds, Science with a Next Generation Very Large Array. Neutral Atomic Hydrogen in the Local Universe, Astronomical Society of the Pacific, USA, p. 471
Planck Collaboration XVI 2014, A&A, 566, A54
Putman M. E., Peek J. E. G., Joung M. R., 2012, ARA&A, 50, 491
Rice W. K. M., Lodato G., Armitage P. J., 2005, MNRAS, 364, L56
Röhser T., Kerp J., Lenz D., Winkel B., 2016, A&A, 596, A94
Rubin K. H. R., Prochaska J. X., Koo D. C., Phillips A. C., 2012, ApJ, 747, L26
Saintonge A. et al., 2017, ApJS, 233, 22
Sanderson R. E. et al., 2020, ApJS, 246, 6
Santistevan I. B., Wetzel A., El-Badry K., Bland-Hawthorn J., Boylan-Kolchin M., Bailin J., Faucher-Giguère C.-A., Benincasa S., 2020, MNRAS, 497, 747
Schaye J., 2004, ApJ, 609, 667
Schmidt M., 1963, ApJ, 137, 758
Schmidt T. M., Bigiel F., Klessen R. S., de Blok W. J. G., 2016, MNRAS, 457, 2642
Sommer-Larsen J., 1991, MNRAS, 249, 368
Sparre M., Hayward C. C., Feldmann R., Faucher-Giguère C.-A., Muratov A. L., Kereš D., Hopkins P. F., 2017, MNRAS, 466, 88
Stern J. et al., 2021, ApJ, 911, 88
Stern J., Fielding D., Faucher-Giguère C.-A., Quataert E., 2020, MNRAS, 492, 6042
Stewart K. R. et al., 2017, ApJ, 843, 47
Stewart K. R., Kaufmann T., Bullock J. S., Barton E. J., Maller A. H., Diemand J., Wadsley J., 2011, ApJ, 738, 39
Tacconi L. J. et al., 2018, ApJ, 853, 179
Thompson T. A., Quataert E., Murray N., 2005, ApJ, 630, 167
van de Voort F., Schaye J., Booth C. M., Dalla Vecchia C., 2011b, MNRAS, 415, 2782
van de Voort F., Schaye J., Booth C. M., Haas M. R., Dalla Vecchia C., 2011a, MNRAS, 414, 2458
van den Bergh S., 1962, AJ, 67, 486
van der Walt S., Colbert S. C., Varoquaux G., 2011, Comput. Sci. Eng., 13, 22
Vogt S. S. et al., 1994, Proc. SPIE Conf. Ser. Vol. 2198, HIRES: the High-Resolution Echelle Spectrometer on the Keck 10-m Telescope. SPIE, Bellingham, p. 362
Werk J. K. et al., 2019, ApJ, 887, 89
Wetzel A. R., Hopkins P. F., Kim J.-H., Faucher-Giguère C.-A., Kereš D., Quataert E., 2016, ApJ, 827, L23
Wetzel A. R., Nagai D., 2015, ApJ, 808, 40
Witherspoon C., Wilcots E., Masters K., 2020, American Astronomical Society Meeting Abstracts. American Astronomical Society Meeting Abstracts, 305.14
Wolfe A. M., Gawiser E., Prochaska J. X., 2005, ARA&A, 43, 861
Wong T., Blitz L., Bosma A., 2004, ApJ, 605, 183
Worthey G., Dorman B., Jones L. A., 1996, AJ, 112, 948
Yu S. et al., 2021, MNRAS, 505, 889
Zabl J. et al., 2019, MNRAS, 485, 1961
Zheng Y., Peek J. E. G., Werk J. K., Putman M. E., 2017, ApJ, 834, 179

## APPENDIX A: COMPARISONS BETWEEN CR+, HYDRO+, AND MHD+ RUNS

As discussed in Section 2, the FIRE-2 simulations with MHD and cosmic ray physics (CR+) were used in this study due to their more realistic star formation rates and radial velocities compared with the hydrodynamical only simulations (Hydro+) and the MHD runs without the additional CR physics (MHD+) (Hopkins et al. 2020). In this appendix, we highlight some key differences between the Hydro+, MHD+, and CR+ runs to illustrate that the overall qualitative properties of the gas flows near and inside galactic discs are the same. The three simulation suites are run with the same baryonic mass resolution of $m_{\rm gas} = 7100 M_{\odot}$, and the same maximum spatial resolution and gravitational softening.

All sets of simulations form flat discs with spiral arms, however there are differences in gaseous and kinematic structure (Fig. A1). In general, CR pressure in CR+ runs smooths extreme over- and underdensities outside galaxies. The discs in the CR+ runs also are kinematically colder, owing to lower star formation rates and infall rates in the disc. Differences are clearly seen for **m12i** and **m12f** runs with and without CRs. The Hydro+ and MHD+ runs in these cases have large gaps in the gas distribution, arising from the extreme outward flowing radial velocities that can be seen in Fig. A2.

Similar to the CR+ runs, the Hydro+ and MHD+ runs show gas accreting parallel to the disc and piling up at the disc edge (Section 5.1). The Hydro+ and MHD+ runs, however, show significantly higher accretion rates, mass fluxes, and star formation rates (Table A1). Additionally, the drop in radial speed at the disc edge, which signifies this pile-up, is several times higher in the Hydro+ and MHD+ runs (Fig. A3,A4). This is also obvious in Fig. A2, where radial velocities within the disc and outside the disc are more extreme. The differences in these velocities ultimately arises from the additional pressure support provided by the cosmic rays, which becomes important in the CGM (Chan et al. 2019; Hopkins et al. 2020; Ji et al. 2020). This regulates gas flows in galactic haloes with the net effect of slowing down the rapid gas infall. An indirect effect of lower infall rates are lower gas surface densities and star formation rates, resulting in more quiet kinematics of galactic discs (Chan et al., in preparation).

The structure of accreting gas is qualitatively the same in both runs, with gas accreting on to galactic disc along a funnel shape at relatively small angles with respect to the disc. Gas on large scales tends to be more strongly aligned with the plane of the disc in CR+ runs (Hopkins et al. 2021a). The specific angular momentum of the gas particles in the Hydro+ and MHD+ runs follow closely the rotation

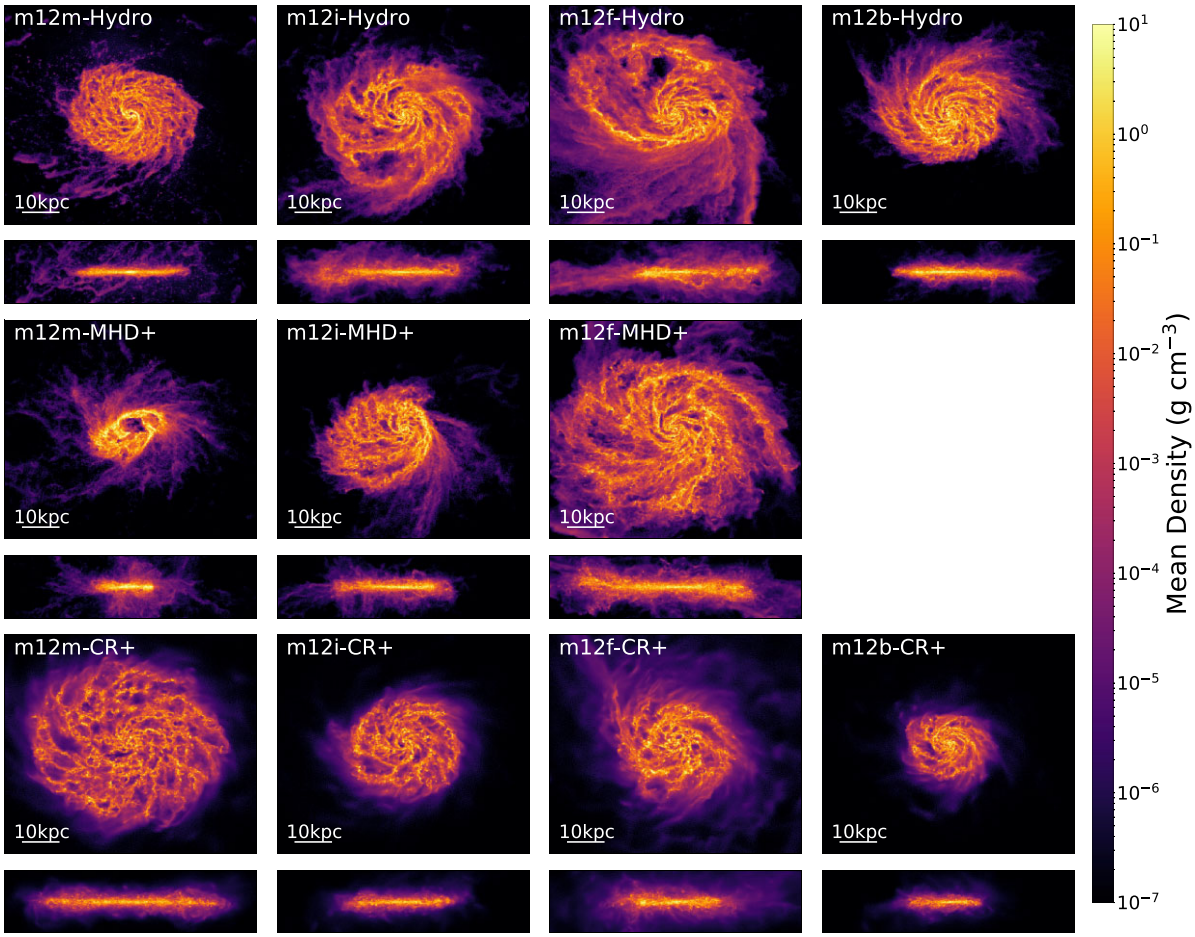


**Figure A1.** Face-on view of average gas density at z = 0. Hydro+ runs are shown on top, runs with MHD but not CRs (MHD+) are shown in the middle, and CR+ are shown on the bottom. The CR+ runs tend to form more cohesive discs on average.

curve for $r<R_{\rm DLA}$, while for $r>R_{\rm DLA}$ gas starts rotating slower than is needed for angular momentum support (Fig. A5). More significant differences are seen in Fig. A6. While the orientation of particle rotation is strongly co-aligned with galactic rotation within the disc and still loosely aligned at higher radii, it drops off more sharply and has much larger spread in specific angular momentum in the Hydro+ runs.

Fig. A7 shows the relative contributions of flows parallel and orthogonal to the disc. As in the CR+ runs, the parallel flows are more consistently inflowing in the Hydro+ and MHD+ runs. They are more chaotic though, largely due to the higher star formation rates.

If observable, the more extreme radial velocities present in the Hydro+ and MHD+ runs would be easier to detect, however, they do not compare as well to observed galactic properties. The star formation rates within these galaxies are slightly higher than expected (Hopkins et al. 2018), fluctuate more significantly over time, and have relatively higher velocity dispersion in the ISM gas (Chan et al., in prepaation). We therefore suggest that detailed findings in the CR runs are better matched to observed $L_*$ galaxies.

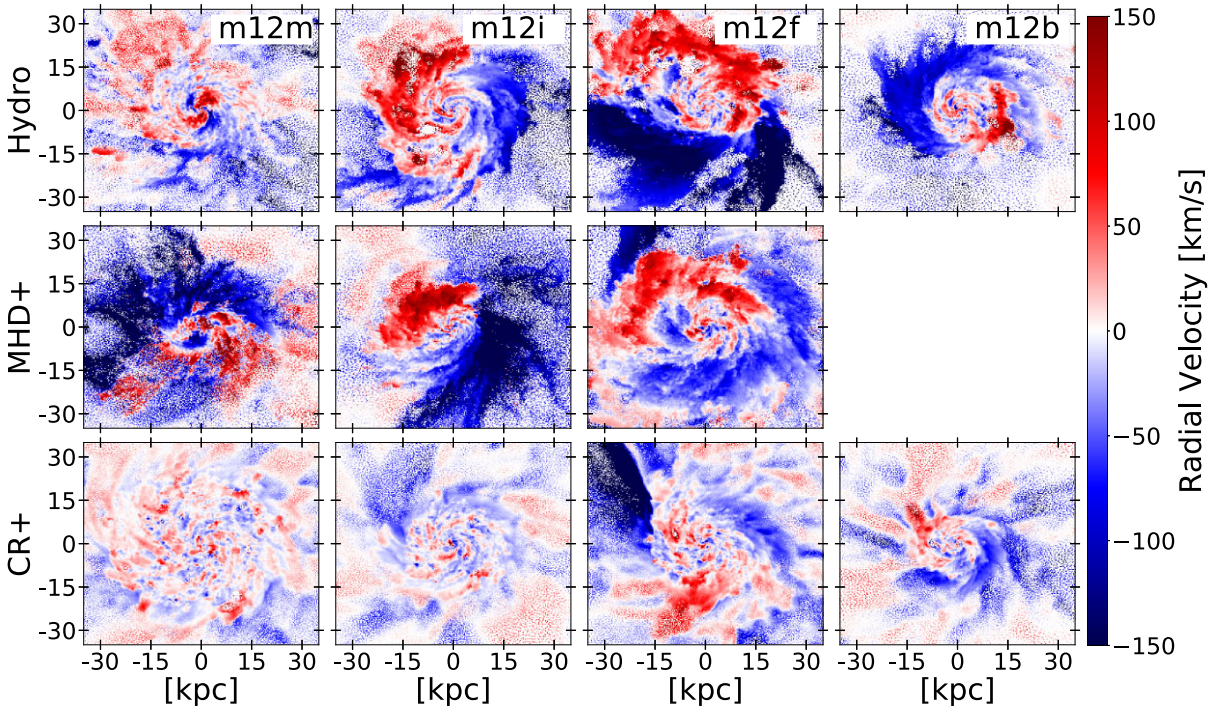


**Figure A2.** Radial velocity maps for the Hydro only runs (Hydro+, top), runs with MHD but not CRs (MHD+, middle), and the CR+ runs (top). Radial velocities in the Hydro+ runs tend to be 2–3 times higher on average, leading to stronger gas flows and less coherent discs.

**Table A1.** Comparison between $R_{\rm DLA}$, stellar mass, total accretion, mass flux through the disc, and total SFR for Hydro+ runs, runs with MHD but no additional CR physics (MHD+), and CR+ runs (presented in the main paper). Accretion, mass flux, and SFR values were averaged from redshift z = 0.2 to 0. Values were calculated as described in Tables 1 and 2. Accretion, mass flux, and SFR values are ∼2 and 4 times higher in the Hydro+ and MHD+ runs, consistent with higher stellar masses.

| Simulation Name | Run | $R_{\rm DLA}$ (kpc) | $M_*$ ($M_\odot$) | Total accretion ($M_\odot$ yr$^{-1}$) | Disk mass flux ($M_\odot$ yr$^{-1}$) | SFR ($M_\odot$ yr$^{-1}$) |
|---|---|---|---|---|---|---|
| **m12m** | Hydro+ | 17.1 | 1e11 | 5.6 ± 6.7 | 11 ± 2 | 15 ± 5 |
| | MHD+ | 11.7 | 1e11 | 6.6 ± 9.9 | 18.5 ± 37.0 | 8.9 ± 2.0 |
| | CR+ | 26.8 | 3e10 | 1.7 ± 0.5 | 2.7 ± 0.4 | 2.5 ± 0.6 |
| **m12i** | Hydro+ | 24.7 | 7e10 | 6.8 ± 3.2 | 6.1 ± 0.9 | 6.6 ± 3.5 |
| | MHD+ | 20.6 | 7e10 | 3.0 ± 3.4 | 13.7 ± 17.5 | 6.5 ± 2.0 |
| | CR+ | 17.1 | 3e10 | 2.2 ± 1.0 | 1.5 ± 0.3 | 1.7 ± 1.5 |
| **m12f** | Hydro+ | 29.3 | 8e10 | 12.5 ± 15.9 | 9.2 ± 1.2 | 7.5 ± 3.4 |
| | MHD+ | 30.1 | 8e10 | 9.8 ± 6.4 | 11.2 ± 23.9 | 7.1 ± 1.6 |
| | CR+ | 18.3 | 4e10 | 3.7 ± 10.2 | 4.4 ± 1.6 | 2.3 ± 2.0 |
| **m12b** | Hydro+ | 18.7 | 1e11 | 6.2 ± 5.7 | 6.7 ± 1.3 | 5.4 ± 1.6 |
| | CR+ | 11.7 | 4e10 | 2.9 ± 1.9 | 1.8 ± 0.7 | 1.9 ± 1.3 |

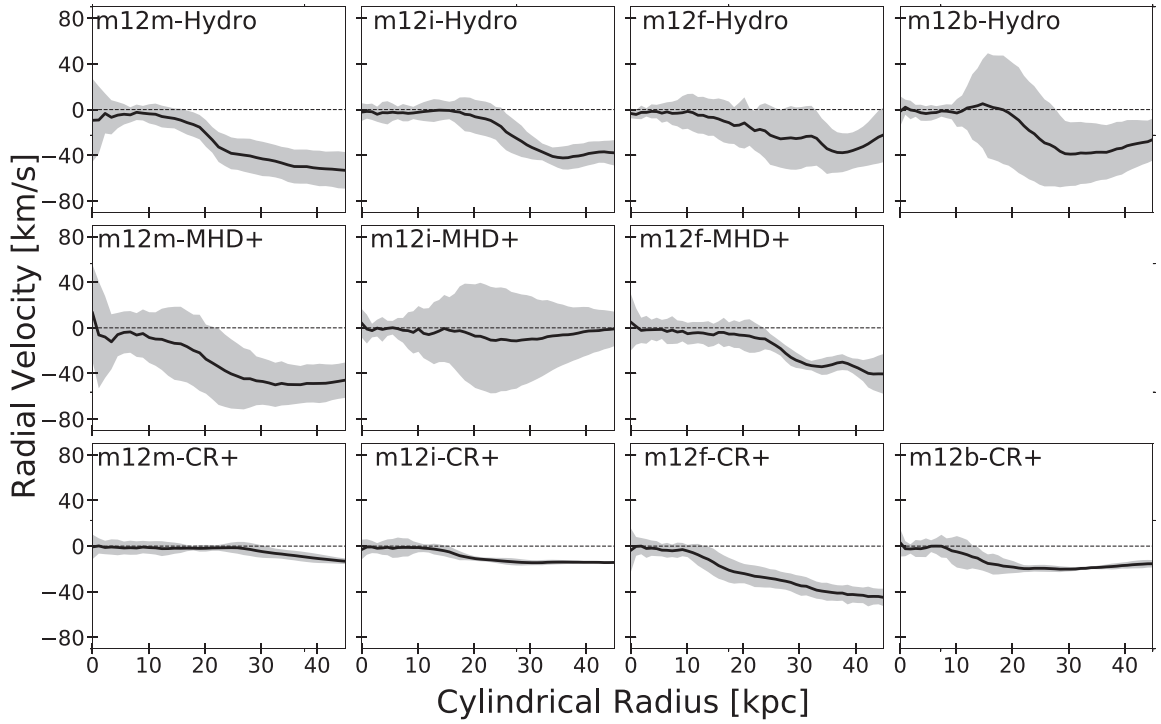


**Figure A3.** Cylindrical radial velocity as a function of cylindrical radial distance from the disc centre for runs with Hydro only (Hydro+, top), with MHD but not CRs (MHD+, middle), and the CR+ runs (bottom). Values were averaged between ±10 kpc as was done in Fig. 4. Runs without cosmic rays tend to have more extreme radial velocity values on average, as well as larger deviations. The same general trend of gas slowing down as it reaches the disc edge remains between both runs.

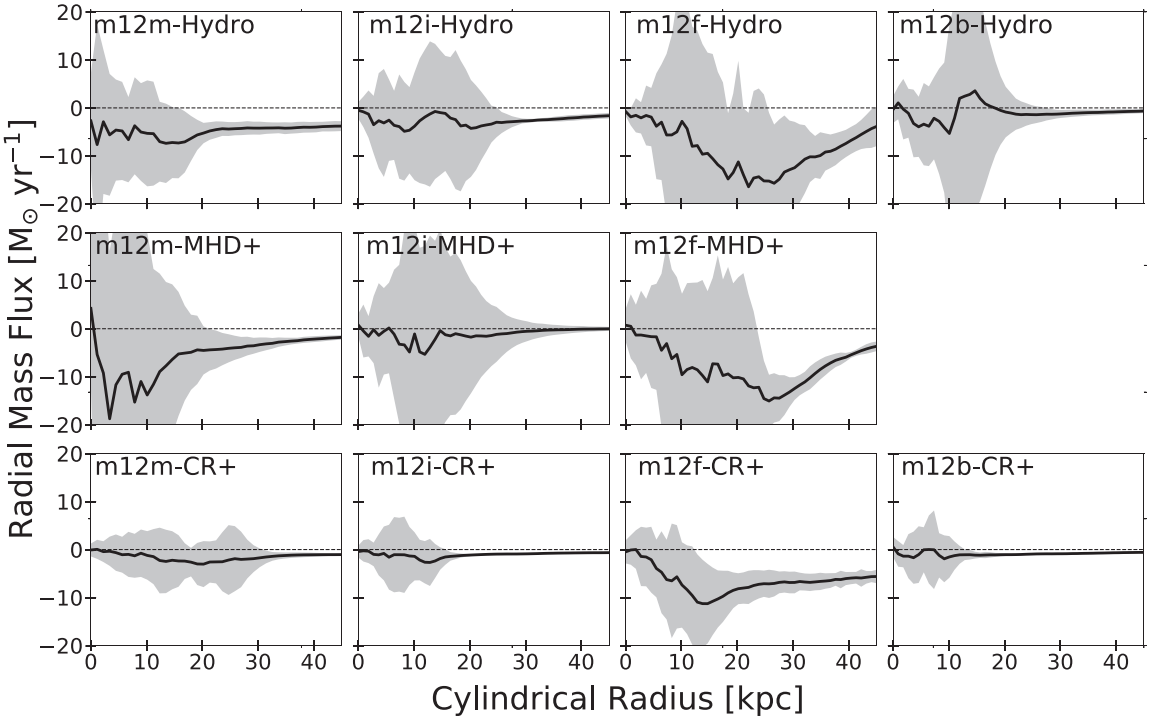


**Figure A4.** Cylindrical radial mass flux as a function of cylindrical radial distance from the disc centre for runs with Hydro only (Hydro+, top), with MHD but not CRs (MHD+, middle), and the CR+ runs (bottom). Values were averaged between ±10 kpc as was done in Fig. 4. Runs without cosmic rays tend to have more extreme radial mass fluxes on average, as well as larger deviations.

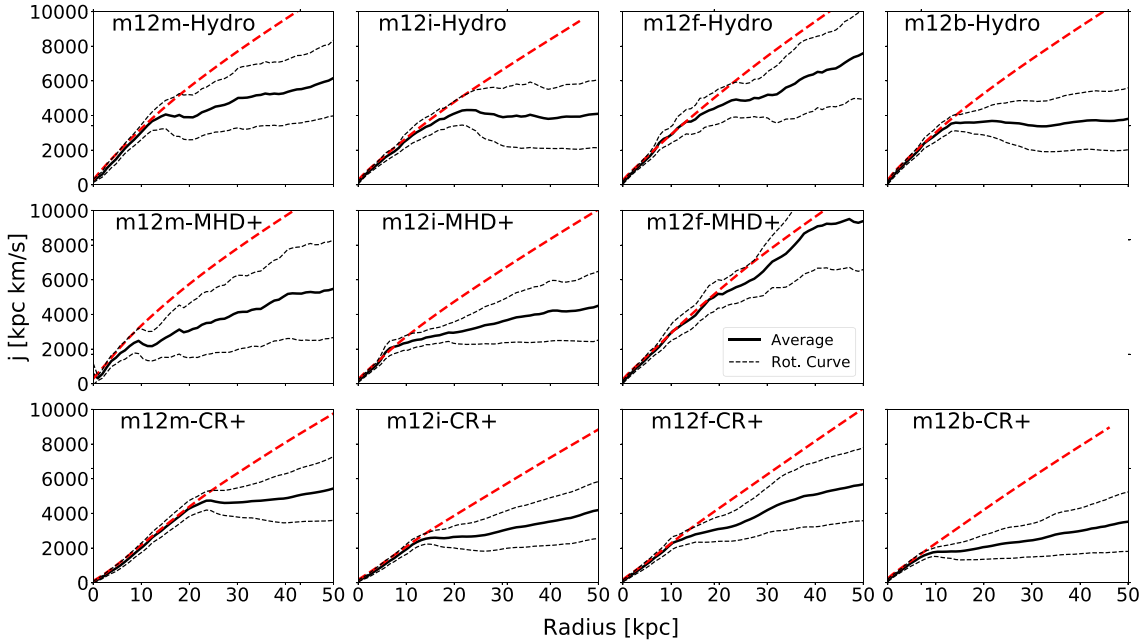


**Figure A5.** Specific angular momentum curves dependence on galactocentric radius for runs with Hydro only (Hydro+, top), with MHD but not CRs (MHD+, middle), and the CR+ runs (bottom). The thick red dashed lines show the specific angular momentum needed for rotational support. The thin black dashed lines show the standard deviation around the mean. All simulation suites show a tight distribution at $r \leq R_{\rm DLA}$ where gas is fully rotationally supported. At larger radii, gas specific angular momentum is lower than needed for rotational support (as expected for the gas that is infalling) and deviations amongst particles at fixed radius are larger.

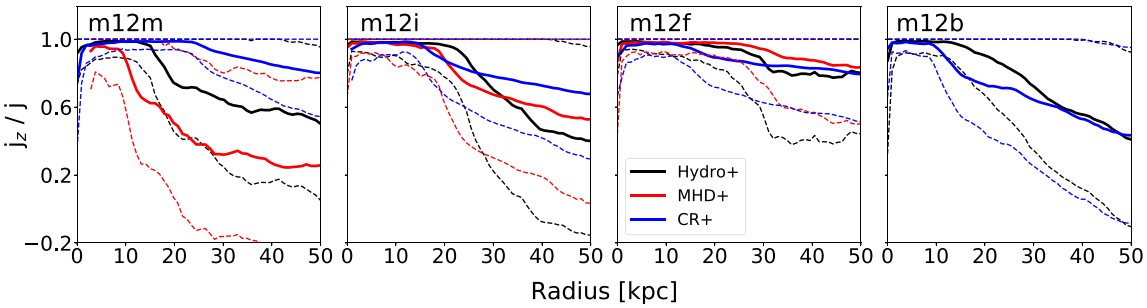


**Figure A6.** Normalized z-components of the specific angular momenta: fraction of the total angular momentum in each radial bin in the direction of galactic angular momentum for runs with Hydro only (Hydro+, black), with MHD but not CRs (MHD+, red), and the CR+ runs (blue). The dashed lines show the standard deviation around the mean. Runs with cosmic rays tend to corotate more strongly on average, even out to large radii.

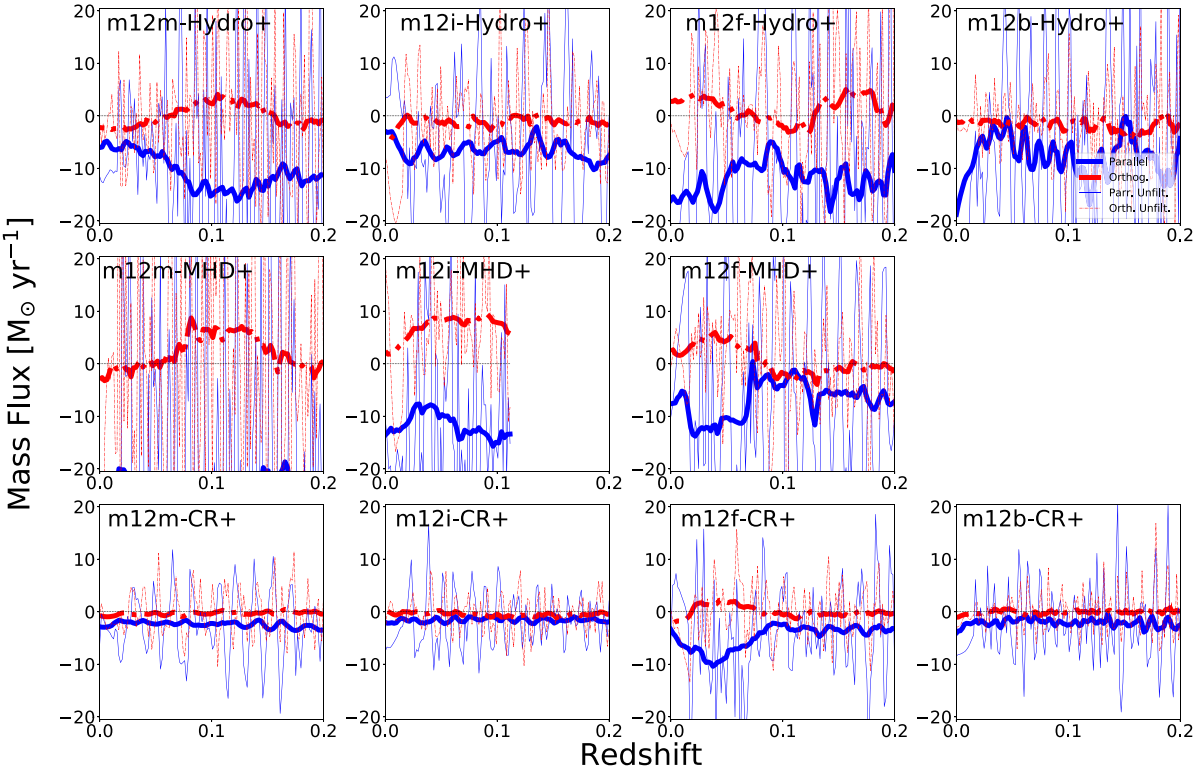


**Figure A7.** Mass fluxes parallel and orthogonal to galactic discs. Negative values represent in-flowing material. Parallel mass fluxes (blue) are measured within 1 scale height of the disc through a 0.5 kpc radial bin centred at 0.5 $R_{\rm DLA}$. Orthogonal mass fluxes (on to the disc plane; red) are measured within 0.5 $R_{\rm DLA}$ in a 0.5 kpc vertical bin at 1 scale height above the disc. Both $R_{\rm DLA}$ and scale heights were calculated at each snapshot to account for disc growth over time. Thick lines are smoothed using a moving average filter with a window width equal to the dynamical time for each galaxy in order to suppress oscillations. Unfiltered values are shown by thin lines. In general, the parallel flows in all runs are a more consistent source of inflow than the orthogonal flows. The MHD+ and Hydro+ runs tend to be more chaotic largely due to higher star formation rates.

## APPENDIX B: MISC. FIGURES

This appendix shows various supplementary figures to the main text. Fig. B1 is a histogram of where the accreting particle sample (see Section 3.2) joins the disc weighted by area. It is the same as Fig. 6, but each bin is divided by the area of its annulus. This naturally flattens the curve in all cases, in broad agreement with semianalytic models of galactic disc evolution that require such flat distributions to match a broad range of disc scaling relations (Forbes et al. 2019), although **m12m** still peaks near the disc edge.

Fig. B2 is a histogram that shows the radial velocities of individual gas elements within the disc averaged over time. This gives the same average values as the azimuthal averaging (Fig. 4), although some particles move with average velocities up to 20 km s$^{-1}$.

Fig. B3 shows the face on average vertical velocities (orthogonal to the disc). Blue/negative values represent inflow both above and below the disc, while red/positive values represent outflows (i.e. velocities of particles below the disc were multiplied by −1 to consistently represent inflow/outflow when averaged together). Of particular note, we can see small regions of large outflows near the disc centres, particularly in **m12i** and **m12f**, as would be expected from concentrated stellar feedback.

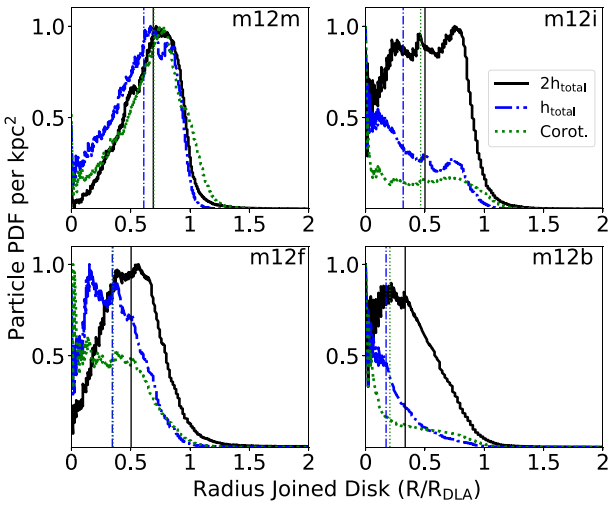


**Figure B1.** Version of Fig. 6 but showing accretion per unit face-on area as a function of galactocentric distance in the disc plane. We again show results for three different accretion definitions based on the scale-height of the gas and level of rotational support. The vertical lines show the median of the distribution. While radial distribution of gas accretion is clearly biased towards infall in the outskirts of galaxies (see Fig. 6), accretion per unit area is more flat. Compact disc of **m12b** exhibit more centrally concentrated distribution, while the most extended disc **m12m** still shows accretion peaked in the outskirts.

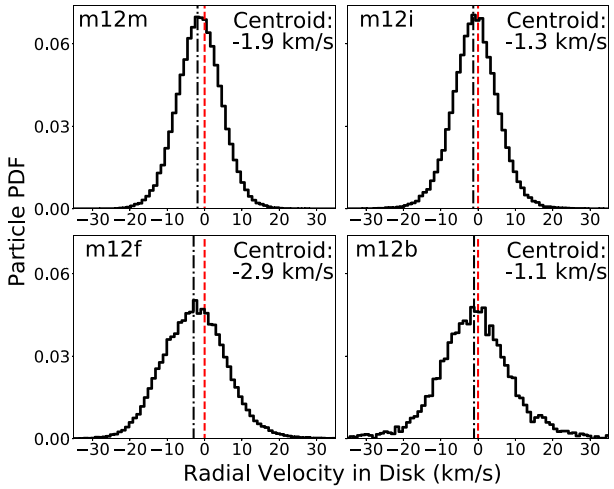


**Figure B2.** Radial velocities of a selection of gas particles within $0.25R_{\rm DLA} \leq r \leq R_{\rm DLA}$. Velocities for individual gas elements were averaged over 1 dynamical time (Table 1) in order to reduce the effects of spiral arm motion. Velocities of all gas elements are biased inwards and are on average 1–3 km $s^{-1}$.

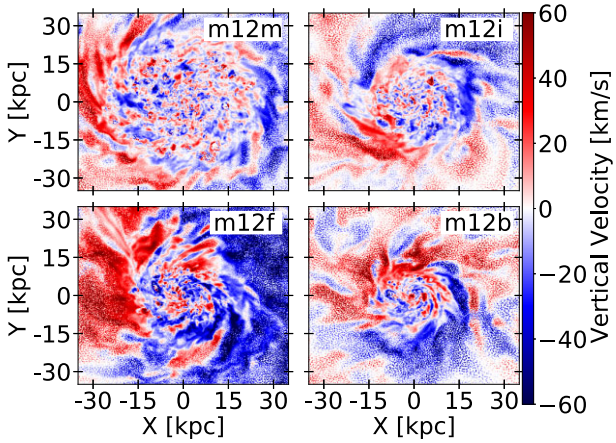


**Figure B3.** Face on views showing averaged vertical velocities for all gas within 1.5 kpc of the disc plane at z = 0. For corresponding parallel velocities, see Fig. 3.

## APPENDIX C: RESOLUTION COMPARISONS

This section briefly compares a lower resolution CR+ simulation run with original gas particles mass of $m_{\rm gas} \sim 56000\,{\rm M}_\odot$ (cr56000) to the runs used as default in this paper with $m_{\rm gas} \sim 7000\,{\rm M}_\odot$ (cr7000). Fig. C1 compares how the specific angular momentum of gas changes with radius. Curves are very similar in all cases, following the rotation curve tightly within the disc, and flattening outside the disc. Overall, we do not see any strong resolution trends in qualitative and quantitative nature of gas infall close to galactic discs.

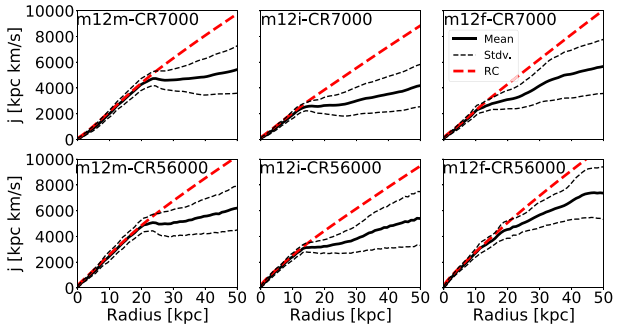


**Figure C1.** Comparison between mass-weighted average specific angular momentum curves as a function of spherical radius between res7000 and res56000 runs. Results are qualitatively similar.

This paper has been typeset from a TEX/LATEX file prepared by the author.